Frequency & Time:

Proceedings of the 4th IFSA Frequency & Time Conference

21-23 September 2022
Corfu, Greece

Edited by Sergey Y. Yurish

IFSA Publishing

Sergey Y. Yurish, *Editor*
Frequency & Time
IFTC' 2022 Conference Proceedings

Copyright © 2022
by International Frequency Sensor Association (IFSA) Publishing, S. L.

E-mail (for orders and customer service enquires): ifsa.books@sensorsportal.com

Visit our Home Page on http://www.sensorsportal.com

All rights reserved. This work may not be translated or copied in whole or in part without the written permission of the publisher (IFSA Publishing, S. L., Barcelona, Spain).

Neither the authors nor International Frequency Sensor Association Publishing accept any responsibility or liability for loss or damage occasioned to any person or property through using the material, instructions, methods or ideas contained herein, or acting or refraining from acting as a result of such use.

The use in this publication of trade names, trademarks, service marks, and similar terms, even if they are not identifies as such, is not to be taken as an expression of opinion as to whether or not they are subject to proprietary rights.

ISBN: 978-84-09-43855-6
BN-202120915-XX
BIC: TBMM

Contents

Foreword

On behalf of the IFTC' 2022 Organizing Committees, we introduce with pleasure these proceedings devoted to contributions from the 4th IFSA Frequency & Time Conference held in Corfu, Greece The conference is organized by the International Frequency Sensor Association (IFSA) - one of the major professional, non-profit association serving for industry and academy more than 20 years in technical cooperation with IFSA Publishing, S.L..

The proceedings contains all papers of both: oral and poster presentations (in-person and virtual) and keynote presentations. We hope that these proceedings will give readers an excellent overview of important and diversity topics discussed at the conference.

We thank all authors for submitting their latest work, thus contributing to the excellent technical contents of the Conference. Especially, we would like to thank the individuals and organizations that worked together diligently to make this Conference a success, and to the members of the International Program Committee for the thorough and careful review of the papers. It is important to point out that the great majority of the efforts in organizing the technical program of the Conference came from volunteers.

Prof., Dr. Sergey Y. Yurish
IFTC' 2022 Chairman

(001)

High Performance Industrial Cesium Beam Clock

P. Berthoud [1], M. Haldimann [1], F. Kroll [1] and V. Dolgovskiy [1]
[1] Oscilloquartz SA, Av. Des Paquiers 1, 2072 St-Blaise, Switzerland
Tel.: + 41 32 722 55 55, fax: + 41 32 722 55 56
E-mail: berthoud@oscilloquartz.com

Summary: Oscilloquartz SA has developed a high performance Cesium beam clock based on the optical pumping technology instead of the traditional magnetic deflection. It allows to improve the clock frequency stability and accuracy without compromising on its lifetime (10 years). This clock fits in a standard 19'' rack, 133 mm high (3U) and is 450 mm deep. Its frequency stability averages as $\sigma_y(\tau)$ = 4E-12 $\tau^{-1/2}$ and reaches 4E-15 at τ=1E6 s for more than 50 days of measurement. When operated as a free running clock, its time interval error remains within ±6 ns over this period.

This product has been designed for high end industrial applications, such as frequency metrology, time scale, or Position Navigation and Timing (PNT). This latter application becomes more and more critical due to the increase of timing holdover duration in case of outage of the Global Navigation Satellite Systems (solar storms, jamming, spoofing).

Keywords: Atomic clock, Cesium, Optical pumping, Laser.

1. Introduction

Although numerous developments have been made at laboratory level to develop more stable and more accurate atomic frequency standards, cesium thermal beam frequency standards remain the reference technology for industrial applications (telecommunication, defence, metrology, time scales). For more than 30 years, the atomic resonator technology has been using the magnetic deflection to select the proper hyperfine energy levels of cesium atoms, which has led to trade-off between the clock frequency stability and the cesium tube lifetime regarding the cesium source consumption.

A technological alternative has been proposed already in the late 1980's with the use of the optical pumping of the cesium beam [1] to increase the useful cesium flux by typically a factor 100 and so forth the clock short-term stability by a factor 10 towards 3E-12 $\tau^{-1/2}$ without reducing the tube lifetime (10 years). Numerous attempts have been made to industrialize this laboratory technology [2, 3], but no products are commercially available with this strongly improved stability [4].

Oscilloquartz SA, Switzerland has developed an industrial optically-pumped cesium beam clock, which fits is a standard 19'' rack, 133 mm high (3U) and is 450 mm deep. It weighs 23 kg and consumes 35 W at ambient temperature (Fig. 1).

The thermal Cesium vacuum tube is operated at a standard oven temperature allowing to guarantee an operational lifetime of 10 years. The optical pumping and detection processes are achieved with a single narrow band laser diode module without any other active optical components (e.g. optical modulator), which improves the clock reliability. The clock signal processing is fully digital allowing to compensate for numerous environmental perturbations, such as thermal and magnetic sensitivities. In comparison with the standard magnetically-deflected Cesium tube, the optically-pumped Cesium tube significantly improves its short-term stability, but might lack of a long-term stability due to the AC Stark shift (also called the atomic frequency light shift). This effect is well knows in other optical standards (cell type Rb standards, optical clocks …), but it has been proven to also affect the frequency stability of compact thermal beam tube [5]. Indeed, as the travelling atoms throughout the tube are continuously subjected to the infrared resonant light, their reference frequency and so forth the clock output frequency might become unstable if the light shift is not properly managed. Thanks to an appropriate algorithm (patent pending), the influence of this light shift effect has been significantly reduced, allowing to improve the clock long-term stability. Moreover its frequency sensitivity to the external temperature variation has been significantly reduced. However the price to pay is a slightly reduced short-term stability (-25 %) compared to the same clock operated without this light-shift compensation algorithm.

Fig. 1. High performance optically-pumped cesium beam clock OSA-3300. This clocks fits in a standard 19'' rack, 133 mm high (3U) and is 450 mm deep. It weighs 23 kg and consumes 35 W at ambient temperature.

2. Results

The Fig. 2 shows the measured frequency stability of the OSA-3300 cesium clock compared to an active hydrogen maser. This clock has been operated autonomously in standard lab conditions. Its frequency

stability expressed as the overlapping Allan deviation averages as $\sigma_y(\tau) = 4E\text{-}12\ \tau^{-1/2}$ and reaches 4E-15 at τ=1E6 s for more than 50 days of measurement. Compared to commercially available high performance Cesium beam clock (Microchip 5071A), the frequency stability is improved by a factor 2 for a twice longer tube design lifetime.

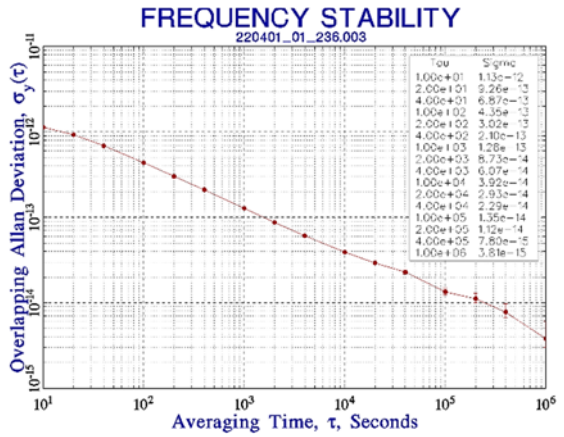

Fig. 2. Frequency stability of a high performance optically-pumped cesium beam clock OSA-3300 measured against an active hydrogen maser. The short-term stability averages as $\sigma_y(\tau) = 4E\text{-}12\ \tau^{-1/2}$ and reaches 4E-15 for an averaging time τ=1E6 s.

The Fig. 3 shows the evolution of the Time Internal Error (TIE) of the OSA-3300 free running clock compared to the reference maser. After 50 days of operation, the TIE has been kept within ± 6 ns. Such performances demonstrate the capability of the optically-pumped Cesium beam clock OSA-3300 for numerous time and frequency applications, such as frequency metrology, time scales, Position Navigation and Timing (PNT) … This last application becomes more and more critical in case of Global Navigation Satellite System outage and this clock can provide excellent time keeping capabilities for extended holdover periods.

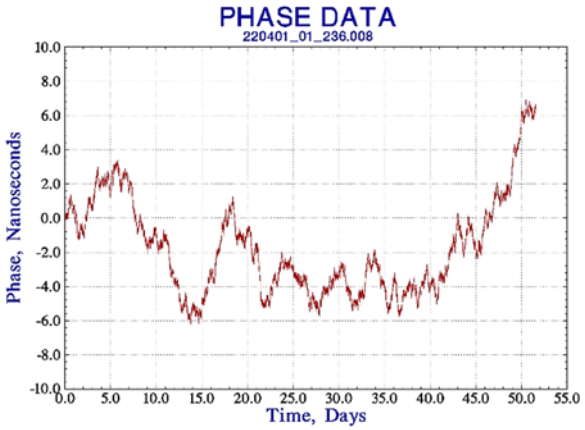

Fig. 3. The Time Interval Error (TIE) of the OSA-3300 free running clock compared to the reference maser remains within ± 6 ns for more than 50 days of operation.

Such performances demonstrate the capability of the optically-pumped Cesium beam clock OSA-3300 for numerous time and frequency applications, such as frequency metrology, time scales, Position Navigation and Timing (PNT) … This last application becomes more and more critical in case of Global Navigation Satellite System outage and this clock can provide excellent time keeping capabilities for extended holdover periods.

3. Conclusion

Oscilloquartz SA has developed and commercially released a high performance thermal Cesium beam clock using the optical pumping instead of the traditional magnetic deflection. In order to optimize the clock reliability, a single monolithic and narrow band laser is used without any other active optical element (e.g. acousto-optic modulator). The most important performance parameter is its output frequency stability: its overlapped Allan standard deviation is $\sigma_y(\tau) = 4E\text{-}12\ \tau^{-1/2}$ and reaches 4E-15 at τ=1E6 s for more than 50 days of measurement, which is twice better and for a twice longer Cesium tube lifetime compared to the industrial benchmark clock (Microchip HP 5071A).

The whole clock fits in a standard 19" rack, 133 mm high (3U) and 450 mm deep. It weighs 23 kg and consumes 35 W in standard lab conditions.

Such clock has been designed to address high end industrial applications, such as frequency metrology, time scales or Position Navigation and Timing (PNT). In case of outages of the Global Navigation Satellite Systems (solar storms, jamming, spoofing), the optically-pumped Cesium clock is a performing backup solution for keeping accurate timing over long hold over period.

References

[1] G. Avila et al., State selection in a cesium beam by laser diode optical pumping, *Phys. Rev. A*, Vol. 36, Issue 8, 1987, pp. 3719-3728.

[2] R. Lutwak, Optically pumped cesium-beam frequency standard for GPS-III, in *Proceedings of the Precise Time and Time Interval Meeting (PTTI 2001)*, Long Beach, CA, USA, 27-29 November 2001, pp. 19-32.

[3] C. Sallot et al. 3E-12 $\tau^{-1/2}$ on industrial prototype optically pumped cesium beam frequency standard, in *Proceedings of the Joint meeting IEEE-IFCS / EFTF 2003*, St Petersburg, FL, USA, 4-8 May 2003, pp. 100-104.

[4] Y. Cao et al. A merchandized optically pumped cesium atomic clock, in *Proceedings of the Joint meeting EFTF / IEEE IFCS 2017*, Besançon, France, 9-13 July 2017, pp. 618-621.

[5] A. Brillet, Evaluation of the light shifts in an optically pumped cesium beam frequency standard, *Metrologia*, Vol. 17, 1981, pp. 147-150.

(003)

Influence of Multiple Valence States and Lattice Locations of Sb and Mn co-Dopants on the Piezoelectric Behavior of PZT Ceramics

L. Amarande [1], C. F. Miclea, M. C. Cioangher, V. Toma, I. Pasuk, M. Stefan, C. Negrila and A. C. Joita

[1] National Institute of Materials Physics, 405A Atomistilor, 077125 Magurele, Romania
Tel.: + 40-(0)213690185, fax: + 40-(0)21-3690177
E-mail: amarande@infim.ro

Summary: The influences of multiple valence states and lattice locations of Sb and Mn co-dopants on the piezoelectric behavior of PZT ceramics, were investigated. The following compositions: $Pb_x(Mn_{0.017}Sb_{0.033}Zr_{0.48}Ti_{0.47})O_3$ with x =0.96; 0.98; 1; 1.02; 1.04, were prepared by conventional ceramic technology. The antimony valence state was found to be 3+, in all materials, by X-ray Photoelectron Spectroscopy. The valence of manganese and its variation upon the lead concentration was studied by Electron Paramagnetic Resonance method, which found reduced Mn^{2+} concentrations in the compositions with lead deficit. Structural investigations by X-ray Diffraction provided the lattice parameters and the concentrations of the tetragonal and rhombohedral phases, which were in agreement with the electromechanical, dielectric and ferroelectric properties of the ceramics, corresponding to a hard piezoelectric behavior of these materials. The hardening is attributed to the presence of the large sized Mn^{2+} ions, localized at B-sites, which compensate for the charge of Sb^{3+} ions, predominantly localized, as donors, at the Pb^{2+} site, and not at the B-site as formerly assumed.

Keywords: PZT ceramics, Sb-Mn co-doping, Charge compensation, Piezoelectric properties, Ferroelectric properties.

1. Introduction

Among ferroelectric materials, lead titanate zirconate (PZT) is one of the most preferred in applications, due to its outstanding piezoelectric performances, related to the choice of dopants and Ti/Zr ratio, which can induce hard or soft piezoelectric response (properties). The use of co-dopants enlarges the possibility to adjust these properties, by correlating their lattice position with the valence state.

In this regard, the aim of the present work was to investigate the effect of two co-dopants with multiple valence states and lattice locations, on the piezoelectric, dielectric and ferroelectric properties of PZT ceramics, in terms of their possible mutual charge compensation. Mn is one of them, which can substitute for Ti /Zr ions on the B-site, as an acceptor or isovalent dopant, by easily changing its valence state from 2+, to 3+ or 4+ [1]. Sb, with 3+ and 5+ valences, is the second co-dopant. It can enter both cationic sites of the perovskite lattice, as a substitute of Pb^{2+} [2-5], on the A-site, or of Ti^{4+}/ Zr^{4+} on the B-site [6-10], or on both sites in the same compound [11].

2. Materials Preparation and Measurements

PZT ceramics with the following compositions: $Pb_x(Mn_{0.017}Sb_{0.033}Zr_{0.48}Ti_{0.47})O_3$ with x =0.96; 0.98; 1; 1.02; 1.04, denoted PZT1-PZT5, were prepared using the conventional ceramic method, assuming that Sb^{3+} enters the B-site only. They were synthesized at 900°C for 2h, by the solid state reaction of the precursors powders, then sintered at 1200 °C for 2h. Polished ceramic discs of 10/1 mm were silver paste electroded and subsequently poled in a DC electric field of 40 kV/cm, at 170 °C, in a silicon oil bath.

Morpho-structural investigations were carried out by scanning electron microscopy (SEM) and X-ray Diffraction (XRD), respectively. The dielectric and electromechanical properties were revealed by impedance measurements and the ferroelectric characteristics by measuring the electrical polarization *P* versus the applied electric field *E*. The valences of Sb and Mn were studied by X-ray Photoelectron Spectroscopy (XPS) and by Electron Paramagnetic Resonance method (EPR), respectively.

3. Results and Discussion

The structure of PZT ceramics is revealed by the XRD diffractograms, shown in Fig. 1. They indicate the presence of both tetragonal and rhombohedral phases, as well as of a small amount (< 3 wt%) of secondary ZrO_2 phase, only in PZT1 and PZT2. The concentration of the tetragonal phase decreases from about 85 wt% in PZT1 and PZT2, to 65-70 wt% in the rest of compositions, upon increasing amount of lead, while the rhombohedral phase has an opposite trend. The dependence of the lattice parameters is in agreement with that of the phases concentrations, i.e. the *a* parameter of PZT1 and PZT2 has lower values compared to the rest of the materials, while the *c* parameter has the opposite trend. This corresponds to an increased lattice tetragonality in materials with lead deficit, which is consistent with the highest amount of tetragonal phase.

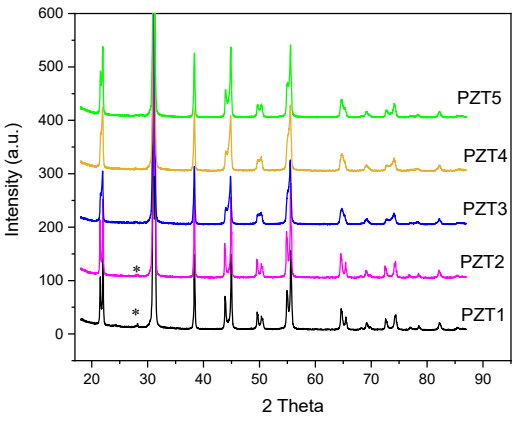

Fig. 1. XRD diffractograms of PZT ceramics

The dielectric constant increases from 830 to 1000, and the dissipation factor shows a slight increase from 0.4% to 0.53%, upon the increasing lead content. The electromechanical coupling factor k_p, and the mechanical quality factor Q_{mp}, of the radial vibration mode of a disc shaped piezoceramic resonator, were determined, by impedance measurements, in the resonance-antiresonance band of this mode. These parameters characterize the electromechanical response of the material. PZT1 and PZT2 have lower values of k_p (0.44-0.48) compared to PZT3-PZT5, with k_p of 0.58. Q_{mp} values are between 950 and 1100, the highest value corresponding to PZT1 and PZT2. The evolution of these two parameters indicates a hard type piezoelectric behavior of these materials.

The P-E hysteresis loops were registered before and after ceramic poling, to investigate the ferroelectric properties. Non-saturated "pinched" loops, with low maximum and remnant polarizations, were obtained before poling, as shown in Fig. 2.

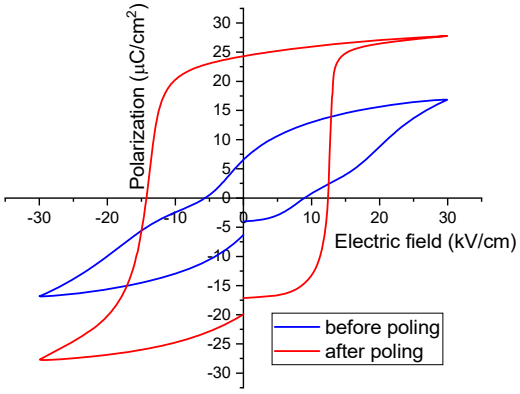

Fig. 2. P-E hysteresis loops of PZT3 ceramic, before and after poling.

They are typical for hard piezoelectric materials. After poling, the loop shape drastically changed, showing an increased area, coercive fields, maximum and remnant polarizations, as shown in Fig. 2. The loops are no longer "pinched", but have an asymmetrical shape and position with respect to the vertical axis, due to the internal field generated by poling. PZT1 and PZT2 have higher asymmetry and coercive fields, but lower remnant polarization compared to PZT3-PZT5. Correlation of all the results of the electrical measurements serves as a clear evidence of the hard type piezoelectric behavior of PZT1-PZT5 ceramics. Among them, PZT1 and PZT2 are harder than the rest of the materials.

XPS measurements found only the 3+ valence state of antimony in all the materials. The valence of the Mn ions was studied by EPR, which revealed the presence of Mn^{2+} ions, whose spectra intensities slightly increased with the increasing amount of lead. This can be explained by a charge compensation mechanism, between the Mn^{2+} ions, localized at the B-sites and a fraction of the Sb^{3+} ions assumed to enter the A-sites, as substitutes for Pb^{2+}. A similar compensation mechanism was reported to be responsible for the properties of Mn an Sb co-doped PZT with different concentrations of Sb [4]. Due to their large size, Mn^{2+} ions, have a pinning effect on the domain walls, reducing their mobility and enhancing the hard type behavior. This was experimentally observed, despite Sb^{3+} being predominantly localized on the A-site, as a donor substitute for Pb^{2+}, which would normally lead to a soft piezoelectric behavior.

4. Conclusions

PZT ceramics with the following compositions: $Pb_x(Mn_{0.017}Sb_{0.033}Zr_{0.48}Ti_{0.47})O_3$ with x =0.96; 0.98; 1; 1.02; 1.04, were prepared by conventional ceramic technology. Structural investigations, performed by XRD showed the presence of the perovskite structure, with both tetragonal and rhombohedral phases. XPS testified only the 3+ valence of antimony and EPR revealed the valences of manganese in correlation with lead concentration.

The dielectric, electromechanical and ferroelectric properties, resulting from the electrical measurements, correspond to a hard piezoelectric behavior, mostly in materials with lead deficit. The hardening is attributed to the presence of large sized Mn^{2+} ions compensating for the charge of Sb^{3+} ions, predominantly localized, as donors, at the Pb^{2+} site, and not at the B-site as previously assumed.

Acknowledgments

The authors acknowledge the financial support of the Romanian National Authority for Scientific Research and Innovation, CNCS UEFISCDI, in the framework of PN-III-P2-2.1-PED-2019-3466 (Contract 433PED/2020) project.

References

[1]. M. D. Glinchuk, I. P. Bikov, V. M. Kurliand, M. Boudys, T. Kala, and K. Nejezchleb. Valency States and Distribution of Manganese Ions in PZT

Ceramics Simultaneously Doped with Mn and Nb, *Phys. Status Solidi A*, Vol. 122, Issue 1, 1990, pp. 341-346.

[2]. T. Zhou, S. Wang, H. Gu, Y. He, A. Kuang, W. Sun, The effect of doping Sb_2O_3 in high d33 • g33 PZT piezoelectric ceramics, *Ferroelectrics*, Vol. 195, 1, 1997, pp. 101-104.

[3]. R. Rai, S. Sharma, Structural and dielectric properties of Sb-doped PLZT ceramics, *Ceramics International,* Vol. 30, 2004, pp. 1295–1299.

[4]. S. Dutta, R. N. P. Choudhary, P. K. Sinha, Electrical properties of antimony doped PLZT ceramics prepared by mixed-oxide route, *J Alloys and Comp*. Vol. 426, Issue 1-2, 2006, pp. 345–351.

[5]. I. Mahmud, M. S. Yoon, S. C. Ur, Antimony Oxide-Doped $0.99Pb(Zr_{0.53}Ti_{0.47})O_3 - 0.01Bi(Y_{1-x}Sb_x)O_3$ Piezoelectric Ceramics for Energy-Harvesting Applications, *Appl. Sci.,* Vol. 7, 2017, pp. 960-14.

[6]. W. Y. Choi, J. H. Ahn, J. H. Choi and H. G. Kim, Fatigue properties of Sb doped PZT thin films deposited by dc reactive sputtering, *Integrated Ferroelectrics*, Vol. 21, 1998, pp. 217-227.

[7]. H. Zheng, I. M. Reaney, W. E. Lee, N. Jones, H. Thomas, Surface Decomposition of Strontium-Doped Soft $PbZrO_3$–$PbTiO_3$, *J. Am. Ceram. Soc*., Vol. 85, Issue 1, 2002, pp. 207–212.

[8]. K. Li, J. Li, D. Cao, J.H. Li, Manganese and Antimony Doped Lead Zirconate Titanate Ceramic Fibers and Fiber/Epoxy 1–3 Composites, *J Composite Mat*, Vol. 42, Issue 11, 2008, pp. 1125–1131.

[9]. S. Eitssayeam, P. Jarupoom, G. Rujijanagul, *High Dielectric and Piezoelectric Properties Observed in Annealed $Pb_{0.88}Sr_{0.12}Zr_{0.54}Ti_{0.44}Sb_{0.02}O_3$ Ceramics*, Ferroelectrics, Vol. 451, 2013, pp. 48–53.

[10]. P. Jaita, C. Kruea-In and G Rujijanagul, Influence of Al_2O_3 Nanoparticles' Incorporation on the Structure and Electrical Properties of $Pb_{0.88}Sr_{0.12}Zr_{0.54}Ti_{0.44}Sb_{0.02}O_3$ Ceramics, *Nanomaterials and Nanotechnology*, Vol. 6, 2016, pp. 27-7.

[11]. L. Amarande, M. C. Cioangher, V. Toma, C. F. Miclea, M. Stefan, et al, Hard/soft effects of multivalence co-dopants in correlation with their location in PZT ceramics, *Ceramics International*, Vol. 47, 2021, pp. 33382–33389.

(004)

A Rauch-Tung-Striebel Algorithm to Improve the End Effect of Static GNSS PPP

Mengshi CHEN [1,2], Haibo YUAN [1,2,3], Jihai ZHANG [1,2,3], Hong Zhang [1,3], Zongyuan LI [1,2] and Yiheng WANG [1,2]

[1] National Time Service Center, Chinese Academy of Sciences, Xi'an 710600, China
[2]University of Chinese Academy of Sciences, Beijing 100049, China,
[3]Key Laboratory of Time and Frequency Primary Standards, Chinese Academy of Sciences, Xi'an 710600, China
Tel.: + 8618220533997
E-mail: chenmengshi@ntsc.ac.cn, yuanhb@ntsc.ac.cn

Summary: Global Navigation Satellite System (GNSS) Precise point positioning (GNSS PPP) is widely applied in positioning and time transfer. How to reduce the convergence time is an important research content of the static PPP technology. An iterative parameter estimation method is proposed to improve the end effect of the basic GNSS PPP technology. The backward filter is used to estimate the Kalman parameters and then the forward filter is processed. The calculated results are performed with the traditional PPP results and the fixed interval smoothed static PPP results. The results show that the root mean square (RMS) of the first 6 hours of data is reduced approximately an order of magnitude and the short term frequency stability is improved approximately an order compared to the traditional PPP, and that the RMS of the last 6 hours of data is reduced approximately 5-20% and the stability is improved approximately 5% compared to the fixed interval smoothed PPP.

Keywords: GNSS PPP, Kalman filter, Time transfer, Frequency and time, Time stability.

1. Introduction

GNSS PPP time comparison technology is an important technology for BIPM to conduct international time transfer [1]. GNSS PPP time transfer technology has been widely applied for low cost, high precision and easy maintenance [2]. Though the traditional static PPP has high accuracy, its convergence time is long [3, 4]. It takes approximately 20 min required for 95 % of solutions to reach a horizontal accuracy of 20 cm or better for static PPP [5, 6]. PPP time transfer has the same result. If only forward filer is used, the first series of data will have poor accuracy. For post-processing calculation, the fixed interval smoother can improve the accuracy. The fixed interval smoother combines forward and backward filter result by the noise matrix. This method can reduce the influence of the one-way filter convergence problem on the calculation of the initial part of the data. But introducing the inverse filtering result directly introduces additional noise, especially in the last part of the result. In order to solve the above problems, the post-processing algorithm based on RTS filtering is investigated in this paper.

2. Method

The traditional static PPP model has multiple model corrections, and it can be written as:

$$\begin{aligned} P_{r,j}^S &= \rho_r^S + c\cdot(dt_r - dt_{s,j}) + T_{r,j}^S + \\ &\quad + I_{r,j}^S + (d_{r,j} - d_j^S) + \varsigma_j + \varepsilon_{r,j}^S(P_{r,j}^S) \\ L_{r,j}^S &= \rho_r^S + c\cdot(dt_r - dt_{s,j}) + T_{r,j}^S - \\ &\quad - I_{r,j}^S + \lambda_j^S(w_{r,j}^S + N_{r,j}^S) + \varsigma_j + \xi_{r,j}^S(L_{r,j}^S) \end{aligned} \quad (1)$$

where $P_{r,j}^S$ and $L_{r,j}^S$ are the code and carrier phase observations, ρ_r^S is the geometric distance, c is the speed of light in vacuum, dt_r and $dt_{s,j}$ are the receiver and satellite clock offset, $T_{r,j}^S$ is the tropospheric delay, $I_{r,j}^S$ is the ionospheric delay, $(d_{r,j} - d_j^S)$ is the hardware latency, λ_j^S is the wavelength of carry phase, $(w_{r,j}^S + N_{r,j}^S)$ is the ambiguity parameter, ς_j is the correction not listed, $\varepsilon_{r,j}^S(P_{r,j}^S)$ and $\xi_{r,j}^S(L_{r,j}^S)$ are the observation noise.

GNSS PPP uses a Kalman filter for parameter estimation. The estimation parameters include antenna coordinates, receiver clock, tropospheric parameters and ambiguity. The Kalman filter model is shown in Equation 2:

$$\begin{aligned} K &= Q*H*(H'*Q*H+R)^{-1} \\ Xp &= X + K*l \\ Qp &= (I - K*H')*Q \end{aligned} \quad (2)$$

where K is the Kalman gain, X and Xp are the state vector, Q and Qp are the covariance matrix of states, l is the innovation (measurement - model), R is the covariance matrix of measurement error, H is the transpose of the design matrix, I is an identity matrix.

For forward filtering, the state parameters and the covariance matrix of the current epoch are calculated from the state parameters and the covariance matrix of the previous epoch. For post processed calculations, the fixed interval smoothed filter is used to combine the result of forward and backward filtering. For a calculation process with a total of N epoch, for epoch k, the state parameters and covariance matrix of epoch k can be calculated from epoch 1 to epoch k by forward filtering, and from epoch n to epoch k by backward filtering. The fixed interval smoothed filter combines the forward and backward results in a smoother, then get the final result. In this way, the results of the unconverted part of the forward filter are improved. However, this calculation introduces additional noise at the end of the data. Thus, a new method based on Rauch-Tung-Striebel (RTS) algorithm is applied in this paper.

First, for a total of N epoch, a series of data from the epoch 1 is calculated by backward filtering. For post processed calculation, sufficient data are used to calculate the covariance matrix and state parameters for epoch 1 with high precision. The station geodetic coordinates, clock offsets, troposphere, ambiguity and corresponding covariance and noise matrices are used as initial information for forward filtering [7]. The result of this forward filtering from epoch 1 to epoch N is the final result. In this way, the influence of convergence at the beginning and the end of the calculation results can be reduced.

3. Data Analysis

The PPP time comparison data UTC(TP)-UTC(ORB) of ORB and TP stations from MJD 59580 to 59587 are shown in follow section. The time comparison results between the two stations published by the International Bureau of Weights and Measures (BIPM) are used as reference.

Benefit from the high accuracy of the calculation results of the traditional static PPP, the results calculated by the above three methods are very close. Therefore, the calculation results are shown as the difference between the clock offset between the two stations calculated by the above three methods and the reference.

The differences of the results of the different methods are shown below. The difference between the forward filtering method and the RTS method are shown in Fig. 2.

As can be seen from Fig. 2, the difference between the results calculated by the two methods and the reference value is on the order of nanoseconds. When compared with the RTS method, the result with forward filter have an obvious convergence process. In the first 6 hours of each day's data, the result of forward filter have large fluctuations. The root mean square (RMS) of the calculated results for the seven days data are used to quantitatively compare the two methods. The RMS of the results using the forward filtering for seven consecutive days is 319 ps, and the RMS of the first 6 hours of each day is 427 ps. The RMS of the results using the RTS method for three consecutive days is 115 ps, and the RMS of the first 6 hours of each day is 88 ps, much better than the forward filter.

The difference between the fixed interval smoother method and the RTS method are shown in Fig. 3.

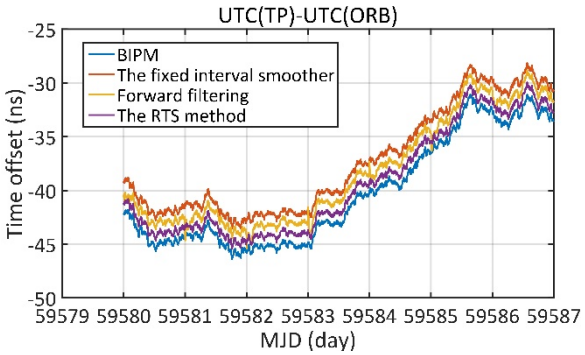

Fig. 1. The time transfer result of UTC(TP)-UTC(ORB) calculated by the above three methods and the results published by the BIPM. The observation data are from TP and ORB laboratories during MJD59580 to MJD59587.

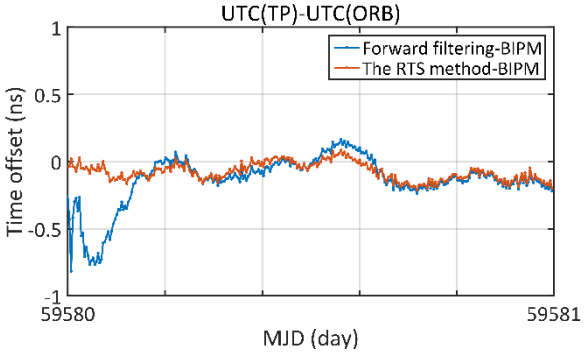

Fig. 2. Difference between time comparison results calculated by RTS algorithm and Forward filter. The observation data are from ORB and TP station, during MJD 59580.

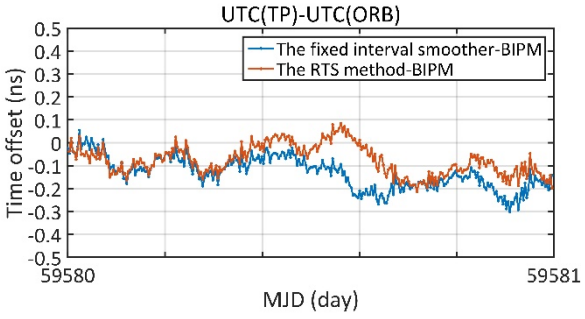

Fig. 3. Difference between time comparison results calculated by RTS algorithm and Fixed interval smoother. The observation data are from ORB and TP station, during MJD 59580.

The results calculated with these two methods are similar, the difference from reference value is within 0.5 ns. The results calculated by the two methods are obviously different in the last half series data. The calculation result of the RTS method is closer to the result calculated by the forward filtering. The RMS of the results with the fixed interval smoother for seven consecutive days is 134 ps, and the RMS of the last 6 hours of each day is 151 ps. The RMS of the results using the RTS method for of the last 6 hours of each day is 138 ps. The result with RTS method has higher accuracy in the last 6 hours of daily data.

The stability analysis is shown in following parts. Overlapping Allen deviation is used to evaluate the frequency stability of the alignment results [8].

Fig. 4 shows the overlapping Allan variance of UTC(TP)-UTC(ORB) calculated by the three methods and published by BIPM. It can be seen that the results of the RTS method and the fixed interval smoother have little difference compared to the value published by BIPM. However, the frequency stability of the results of the forward filtering is an order of magnitude lower than the others at an average time of 1000 seconds. As the average time increases to 100,000 seconds, the frequency stability of the results of the forward filtering raised to the same level as the others. It can be seen that both methods improve the short-term stability and reduce the impact of non-convergence compared with forward filtering.

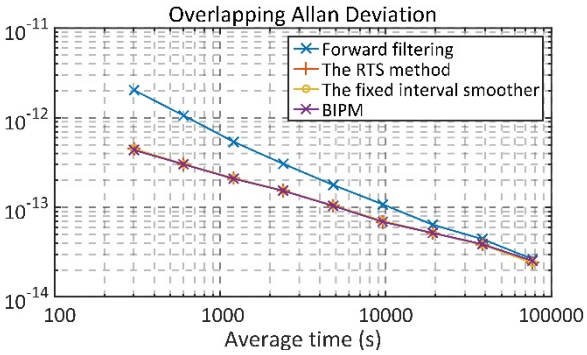

Fig. 4. Overlapping Allan deviation of UTC(TP)-UTC(ORB) calculated by different methods from MJD 58590 to MJD 59587.

Fig. 5 depicts the overlapping Allan variance calculated from 0:00 to 12:00 on MJD 59580 using the three methods. The frequency stability of the results calculated with forward filtering is obviously worse than the other two methods. It can be seen that in the previous part of the calculated data, both methods effectively improve the end effect with forward filtering.

Fig. 6 depicts the overlapping Allan variance calculated from 12:00 to 24:00 on MJD 59580 using the three methods. In the last half part of the calculated data, the results of the three methods have the same order of magnitude of frequency stability. The result calculated by the fixed interval smoother shows slightly worse frequency stability when the average time reach 10000 seconds. This is caused by the direct introduction of backward filtering results.

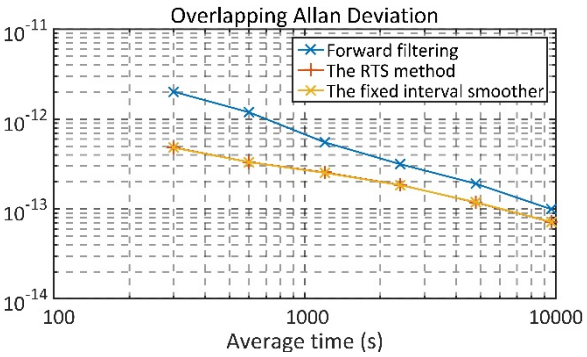

Fig. 5. Overlapping Allan deviation of UTC(TP)-UTC(ORB) calculated by different methods from 0:00 to 12:00 on MJD 59580.

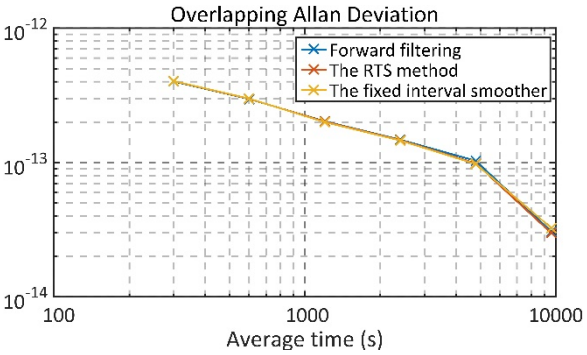

Fig. 6. Overlapping Allan deviation of UTC(TP)-UTC(ORB) calculated by different methods from 12:00 to 24:00 on MJD 59580.

4. Conclusion

For post-processed static PPP, the improved RTS algorithm in this paper can effectively improve calculation results of the start and end parts of a series of data. One-way filter has long converge time. The improved RTS method can effectively reduce the convergence time. When compared with the forward filtering, in the first 6 hours, the RTS algorithm has improved considerable RMS and approximately an order of short term frequency stability. When compared with the fixed interval smoother, in the last 6 hours, the RMS of the results with RTS algorithm are improved at approximately 5-20 %, and the long-term frequency stability are slightly improved.

References

[1]. Kouba, J., Héroux, P., Precise Point Positioning Using IGS Orbit and Clock Products, *GPS Solutions*, 5, 2001, pp. 12–28.

[2]. Zumberge J. F., Heftin M. B., Jefferson D. C., et al., Precise point positioning for the efficient and robust

analysis of GPS data from large networks, *Journal of Geophysical Research,* 1997, 102, B3, pp. 5005-5017.

[3]. Choy, S., Bisnath, S. & Rizos, C. Uncovering common misconceptions in GNSS Precise Point Positioning and its future prospect, *GPS Solutions*, 21, 2017, pp. 13–22.

[4]. Seepersad G., Bisnath S., Challenges in assessing PPP performance, *J Appl Geodesy,* 8, 3, 2014, pp. 205–222.

[5]. Bisnath S., Gao Y., Current state of precise point positioning and future prospects and limitations, in Sideris, M. G. (Ed.), Observing Our Changing Earth, *International Association of Geodesy Symposia, Springer,* Berlin, Heidelberg, 133, 2009, pp. 615–623.

[6]. Hèroux P et al., Products and applications for precise point positioning—moving towards real-time, in *Proceedings of ION GNSS 2004 Meeting,* Long Beach, California, USA, 21–24 September, 2004, pp. 1832–1843.

[7]. Springer Handbook of Global Navigation Satellite Systems. Springer Handbooks, *Springer,* Cham, 2017.

[8]. Allan D. W., Barnes J. A.,. A Modified "Allan Variance" with Increased Oscillator Characterization Ability, in *Proceedings of the Thirty Fifth IEEE Annual Frequency Control Symposium*, 1981, pp. 470-475.

(008)

Security in Packet-Based Time Synchronization Protocols

M. Langer and R. Bermbach
Ostfalia University of Applied Sciences, Salzdahlumer Str. 46/48, 38302 Wolfenbüttel, Germany
Tel.: +49 5331 939 43370, +49 5331 939 42620
E-mail: {mart.langer, r.bermbach}@ostfalia.de

Summary: Time synchronization of many devices and networks is the basis for reliable operation and interoperability. Attacks on time distribution and the synchronization process can therefore lead to serious consequences. In this paper, we provide an overview on the topic of security in time distribution. We show which distribution mechanisms dominate in packet-based networks, which attacks are possible and how they can be mitigated or fended off. In this context, we also present the security protocols that are currently in use or under development.

Keywords: Security, Time synchronization, NTPv4, PTPv2.1, NTS.

1. Introduction

The distribution of time information and the synchronization of devices and networks are the basis for the correct functioning and interoperability of computer systems. Nevertheless, the security aspect has been neglected for a long time, so that attacks on sensitive infrastructures are possible without much effort. However, securing time information poses a particular challenge, since cryptographic measures can degrade synchronicity if used incorrectly, and partly depend on time information themselves (e.g., certificate checks).

In the further course of the paper, Section 2 first provides an overview of common transmission mechanisms and time protocols. Section 3 then addresses the security aspects and describes the countermeasures against known attacks. In the subsequent Section 4, we present the specific security mechanisms in the time protocols and give a brief conclusion in Section 5.

2. Time Distribution Methods and Protocols

Most clocks use a synchronization mechanism to periodically synchronize their own clock to a reference clock with the best possible accuracy and frequency stability (e.g., atomic clock). The aim of synchronization is to continuously align the own clock in phase (time offset) and frequency (drift) with the reference clock and to minimize time deviation.

2.1. Time Distribution and Synchronization

The two most popular methods for distributing time information are one-way and two-way transmission [1]. As depicted in Fig. 1, one-way transmission is typically a broadcast or multicast connection in which a sender (time server/master) periodically transmits time information at one or more receivers (client/slave). An advantage of this method is its simplicity of implementation and high scalability, since the sender does not need to store state information, nor is it necessary to establish a connection. The capturing of the timestamps takes place immediately before sending or after receiving a message. To determine the time offset θ_{OW}, the receiver simply needs to add the transmission duration δ_{OW} to the transmit timestamp T_1 to calculate the difference from the reception time (see equation (1)). However, the transmission time must be estimated or obtained by other means. This in turn leads to the fact that runtime fluctuations have a corresponding negative effect on the synchronicity of the receiver and no prediction regarding the actual age of the time information can be made. In contrast, the two-way transmission depicted in Fig. 2 bases on a request-response principle and enables the receiver to calculate the round-trip time (RTT) δ_{TW} and the time offset θ_{TW} on the basis of four timestamps (see (2) and (3)). Variations in transmission time therefore have less effect on synchronicity and the receiver has the ability to determine the age of the message. Thus, the maximum error is limited to approximately RTT/2 in the case of highly asymmetric runtimes.

$$\theta_{OW} = T_2 - (T_1 + \delta_{OW}) \quad (1)$$

$$\delta TW = (T4 - T1) - (T3 - T2) \quad (2)$$

$$\theta TW = ((T2 - T1) + (T3 - T4)) / 2 \quad (3)$$

Computer systems can typically use two mechanisms to adjust their own clock. The first and simplest option is to modify the time directly. However, this approach is problematic because it may cause scheduled events to be skipped or executed multiple times. For example, inconsistencies can occur in databases if events are no longer in chronological order due to time jumps. A better way of correcting the time is to adjust the speed of the local clock via a control loop, especially if the deviations from the

reference clock are small. This can be done on the basis of a phase-locked loop (PLL) or frequency-locked loop (FLL). The PLL is particularly suitable when synchronization errors due to network fluctuations dominate during time transfer [2, chapter 11.3]. The FLL is used less frequently and is suitable when errors due to oscillator wander dominate. Thus, the local clock slowly converges to the reference clock.

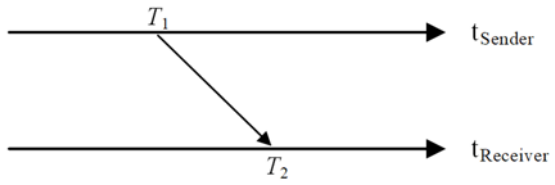

Fig. 1. One-way time transmission.

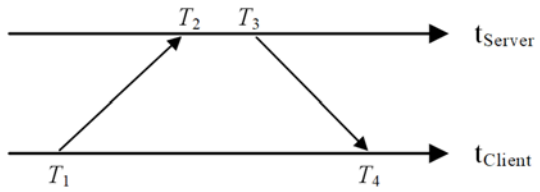

Fig. 2. Two-way time transmission

2.2. Time Protocols

Before we present the security aspects in Section 3, a short introduction to the two most relevant time protocols in packet-based networks follows. These include the Network Time Protocol (NTP) and the Precision Time Protocol (PTP).

2.2.1. Network Time Protocol

The Network Time Protocol is one of the oldest and most widely used Internet protocols. It was developed by D. L. Mills, standardized by the IETF in 1985 as RFC 958 [3], and is available in the current version 4 (NTPv4) [2] since 2010. NTP uses the connectionless User Datagram Protocol (UDP) to transmit time messages mostly over unreliable networks such as the Internet. The communication structure is simple and follows a hierarchical approach, with an atomic clock typically providing the time source at the top. Time servers in the stratum below distribute this time to lower strata, where NTP clients and also other time servers are located. A large number of all NTP connections operate in client-server mode, which is a bidirectional unicast communication between an NTP client and a time server. Here, two-way transmission is used up to four times per minute, in which four timestamps are recorded and transmitted via these messages (see Fig. 2). The NTP packets with the lowest RTT have the smallest errors and serve to synchronize the clock. Due to the hierarchical communication structure in NTP, as well as the use of software timestamps, clients achieve synchronization accuracies in the range of a few milliseconds. The best-known NTP services include the reference implementation NTPD [4], NTPsec [5], Chrony [6] and OpenNTP [7].

2.2.2. Precision Time Protocol

In some application areas, however, the synchronization accuracy provided by NTP is not sufficient. In fields such as electrical power distribution, telecommunications or in the financial sector, accuracies in the micro- or even nanosecond range are required. Such a requirement can be met by the Precision Time Protocol, which was published in 2002 in its first version as IEEE Std. 1588 [8]. Since 2019 it is available in its current version 2.1 (PTPv2.1) [9]. PTP is significantly more complex than NTP and is used almost exclusively in well-managed local networks. Since PTP was developed to achieve high synchronization accuracies, synchronization with an external time server accessible via the Internet is not intended, as the infrastructure itself is not designed for it. Besides open source implementations like Linux PTP [10] and PTPd [11], mainly proprietary solutions exist for the industrial sector.

The PTP network structure is able to change dynamically at any time. At the top of the hierarchy is the so-called Grandmaster, which the PTP network follows. The Grandmaster clock is continuously synchronized with an external, accurate and reliable time source (e.g., atomic clock). The other levels of the hierarchy contain PTP devices (so-called PTP nodes), which synchronize themselves with their neighboring nodes and require at least one PTP-capable Ethernet port. Such ports are called PTP instances and provide hardware support for capturing transmit and receive timestamps. The PTP ports on a device operate independently and could each operates in different states. For example, a port in the slave state receives time information from a master port. If a port wants to use the time information for monitoring purposes and does not want to synchronize with it, then it works in the passive state. The decision of who works as master or slave is determined by the Best Master Clock Algorithm (BMCA). It ensures that the clock with the best accuracy characteristics operate as a master. If a master fails or a slave has better clock parameters, the BMCA automatically changes the hierarchy.

PTP distinguishes between different clock types, transport modes, states and messages. Depending on the PTP message type, the frame rate can be up to 128 PTP packets per second, which can lead to a higher network load, especially in large PTP networks. Delay measurement also distinguishes between the end-to-end (E2E) and peer-to-peer (P2P) methods. However, unlike NTP, the PTP standard does not specify the synchronization mechanism, so these are always implementation-specific solutions.

3. Security Aspects

In recent years, the topic of security has gained more and more relevant. Time information is of particular importance here, as it is not only necessary for the functionality of many tasks in the computer domain, but is also required for the implementation of security mechanisms (e.g., certificate checks). If time information is to be transmitted securely on the basis of such security mechanisms, this can present a particular challenge. However, the widely used time protocols NTP and PTP have paid too little attention to this aspect for a long time.

3.1. Security Threats and Attacker Model

Due to the importance of time information, time protocols and their transmitted messages can be a preferred target for attacks. Due to the unsecured transmission of time information, there are also a large number of vulnerabilities. For NTP, Malhotra et al. describe a series of attacks in [12]. For example, attackers are able to impersonate the time server via spoofing and manipulate intercepted messages at will or inject them into the network themselves. Alternatively, denial of service (DoS) or reflection attacks can be used to overload targeted servers or clients. Mizrahi has summarized the known attacks in RFC 7384 [13] and, among other things, set up a threat model in which the attackers are classified in two categories.

The first category comprises internal attackers, which pose the greatest threat. These are either in possession of authentication keys (e.g., private key), know the encryption key or have access to a trusted segment of the network. Access to such segments, like a PTP node or the key management server, can also be performed by exploiting security vulnerabilities in these devices. The second category covers external attackers who do not possess any keys, nor do they have access or control over a trusted network segment. External attackers can only gain access to authenticated or encrypted traffic. When no protection mechanism is in place, external and internal attackers have the same attack capabilities.

Another distinction must be made based on the positioning of an attacker. A man-in-the-middle (MITM) is typically positioned between two communication partners. Its position allows the listening, dropping, delaying, adding and modifying of protocol packets. This assumes that the MITM has physical access to the network or has control of a network node. Instead of an MITM, injectors can also have access to the network. Although these are not in a MITM position, they are able to generate protocol packets and inject them into the network. With multicast connections, they can also listen to, record and replay protocol packets.

The consequences of an attack on the network and the time synchronization of the devices depend on the type of attack. These can either lead to the failure or inaccessibility of a network node (i.e., DoS), reduce the accuracy of time synchronization or, in the most severe case, establish an incorrect time on the devices (see Table 1). The time synchronicity of unsecured network nodes can be very easily falsified by packet manipulation, spoofing or replay attacks. In contrast, an attack on the entire network can be executed by a rogue time server or by manipulating the time source of a trusted time server. Besides the attack on the time protocol itself, attacks on the underlying network layers (e.g., layer 2 or 3) are also possible. However, even cryptographically secured time protocols offer attack surfaces that must be taken into account. For example, when using asymmetric cryptography or with an inappropriate protocol design, an attacker can create high processor loads on the victim (e.g., on a key management server) by causing many cryptographic operations. Furthermore, there are attacks that cannot be secured with cryptographic methods at all. These include the packet delay attack, which can only be mitigated with monitoring and redundancy mechanisms.

Table 1. Attack on time protocols and countermeasures according to RFC 7384 [13].

Attack	**Impact**			**Attacker Type**				**Countermeasure**
According to RFC 7384	**False Time**	**Accuracy Degrading**	**DoS**	**Internal**		**External**		
				MITM	**Injector**	**MITM**	**Injector**	
Packet manipulation	X			X				Integrity
Spoofing	X			X	X			Authentication
Replay attack	X			X	X			Integrity
Rogue master attack	X			X	X			Authentication /Authorization
Packet interception and removal		X	X	X		X		Monitoring
Packet delay manipulation	X			X		X		Monitoring
L2/L3 DoS attacks			X	X	X	X	X	Monitoring
Cryptographic performance attacks			X	X	X	X	X	Access restrictions / Monitoring
Time protocol DoS attacks			X	X	X			Access restrictions / Monitoring
Grandmaster time source attacks	X			X	X	X	X	Redundancy / Monitoring

3.2. Countermeasures

The defense against attacks is possible on the basis of redundancy, monitoring and cryptography.

3.2.1. Redundancy and Monitoring

For a very long time, attempts were made to increase the security of time protocols by bringing in redundancy. The first and obvious means is to use multiple time sources to avoid single source errors. Depending on how the synchronization mechanism handles Byzantine errors, attackers may need to affect packets from all or a majority of these time sources to disrupt client synchronicity. These different time sources should also be accessible through different paths or transmission media (e.g., fiber, wireless, etc.) to be robust against single channel errors. The realization is very simple and increases resilience.

Another possibility is to use time protocols in parallel. As an example in [14], NTP was proposed as a control mechanism for a PTPv2 infrastructure that runs permanently as a watchdog and monitors time synchronicity. If the monitored PTP clock is more than 5 ms out of sync, it automatically switches to NTP as the primary timing protocol. In contrast, Moussa et al. in [15] describe a mechanism to detect delay changes in PTP networks and mitigate such attacks. In [16], virtual clocks were considered instead for plausibility checking. In it, Anwar et al. also define the notion of Quality of Time, in which time uncertainty is inferred based on accuracy, resolution, and stability of the clock. While all these approaches increase the robustness of the client, they are far from being sufficient to establish true security.

3.2.2. Cryptographic Measures and Primitives

By contrast, cryptographic means can be used to fend off the majority of attacks. With regard to time transmission, the main focus is on ensuring the integrity and authenticity of the transmitted messages. Authenticity ensures that these messages come from the originating and expected sender. Integrity protection, on the other hand, allows received messages to be checked for any changes due to transmission errors or manipulation. In order to make this possible, a one-way function is used to equip the payload with a digital fingerprint. Depending on the cryptographic primitive, this has an impact on various properties. Here, we distinguish between hash, Message Authentication Code (MAC) and digital signature.

Hash algorithms represent the first cryptographic primitive for calculating a checksum and are the fastest way to generate integrity protection. The best known of these are MD4, MD5, SHA1, SHA2, SHA3, and BLAKE2, which provide a fixed output size regardless of the input data. Since pure hash algorithms do not use a key and can be generated by anyone, they consequently do not provide authenticity and are thus unsuitable for securing time messages.

MAC algorithms, on the other hand, use symmetric cryptography to provide the necessary authenticity in addition to integrity assurance. The digital fingerprint generated here is called either MAC or Authentication Tag (AuthTag). For this purpose, sender and receiver use a common and pre-shared symmetric key. Only entities in possession of this key are thus able to verify or generate a MAC. This also enables secure communication of entire groups (e.g., for broadcast), in which all trusted peers use the same key as well. However, the authenticity decreases with the increasing size of the group, as these peers are potentially able to manipulate the messages of the other peers. MAC algorithms therefore provide group source authenticity. Hash- or cipher-based algorithms are often used as methods, which are somewhat slower than pure hash functions. The best-known algorithms are CMAC, GMAC and HMAC, which provide a fixed output size and are suitable for securing time messages.

Besides source authenticity, digital signatures additionally realize non-repudiation, so that the sender is always unambiguously identifiable. This is achieved by using an asymmetric key pair, in which a private key is used to generate the signature and a public key for its verification. This procedure usually generates a hash of the message and then encrypts it asymmetrically. Well-known procedures here are DSA, RSA, ECDSA and EdDSA. This method is significantly slower than MAC or hash methods and requires significantly longer keys for the same security strength. The non-repudiation of sent messages is particularly relevant in legal metrology environments to ensure legal certainty. However, digital signatures are only suitable to a limited extent for securing time messages due to the high resource requirements.

Nevertheless, as Table 1 shows, even cryptography does not offer complete protection. Delay attacks in particular are problematic and cannot be easily detected. With two-way synchronization, such attacks can be mitigated because the client can determine the message age and exclude messages with a high RTT from the synchronization process. With one-way time synchronization, it is not possible to determine the packet age, so monitoring mechanisms are necessary.

4. Security in Time Protocols

Securing time protocols is not trivial, since existing security mechanisms are not designed for time transfer and therefore can drastically degrade synchronization accuracies. Time protocols such as NTP and PTP require special security solutions, which are presented in this section.

4.1. Security in NTP

This section covers the security options for NTP which are published as standard. This covers the built-in protection methods in NTP and protocol extensions.

4.1.1 Built-in Security Mechanisms

The first protection mechanism was already established in NTP version 3 [17], which, based on a pre-shared key scheme, secures the NTP messages with a 128-bit long MAC. Although the pre-shared key scheme is considered fundamentally secure, it is rarely used due to poor scalability. In particular, this approach is not practical in client-server mode, since public time servers would have to hold a separate key for each client and would thus be stateful.

The subsequent Autokey procedure [18], which was released along with NTPv4 in June 2010, solved the scaling issues of the pre-shared key scheme. Autokey is a protocol in which the NTP client and server negotiate the symmetric keys automatically, eliminating the need for the administrator to set keys manually. However, an analysis of the Autokey procedure in 2012 [19] revealed many critical design flaws, particularly in the key generation and authentication procedures. For example, a brute force attack on the 32-bit long cookies makes it possible to obtain the key material within a few minutes. Autokey is thus considered broken and insecure.

4.1.2 *Network Time Security*

The results led to a revision of the Autokey protocol, so that the development of Autokey version 2 was started in July 2012 [20]. Due to the bad reputation of the Autokey protocol, it was renamed Network Time Security (NTS) and published as RFC standard 8915 [21] by the IETF in 2020.

NTS focuses on NTPv4 in client-server mode. It does not support the other NTP modes, because they are barely used and require other security mechanisms. NTS separates the communication into two subprotocols, resulting in several protocol phases (see Fig. 3). The first phase is the NTS key establishment (NTS-KE) protocol, which is used between an NTP client and an NTS-KE server. Here, the client uses the Transport Layer Security protocol version 1.3 (TLSv1.3) [22] to establish a secure connection to the key management server. TLS allows the client to easily authenticate the NTS-KE server using certificates and provides a secure channel that encrypts the subsequent communication as well as protects against attacks such as replay or tampering. Via NTS messages, the client and server negotiate the security parameters and keys for the desired NTP time server. In addition, the client also receives cookies, in which this data is also contained in encrypted form and which can only be decrypted by the NTS-KE server and NTP time server. The exchange of this cookie key between NTS-KE server and time server is currently implementation-specific. After the client has received the parameters, the TLS connection is closed and phase 2 begins. Here, the NTP communication takes place, in which the NTP messages are secured with NTS extension fields. The client also transmits a cookie that allows the time server to verify and secure the NTP messages.

NTS is a well scalable and performant security solution for NTP that allows statelessness of time servers and prevents tracking. It uses modern cryptography, minimizes the negative impact on synchronization accuracy and automatically ensures key freshness, while keeping the protocol design as simple and extensible as possible. Since standardization, there are already a number of NTS-secured time servers and NTS-enabled NTP implementations. These include NTP-O [23], NTPsec [5] and Chrony [6].

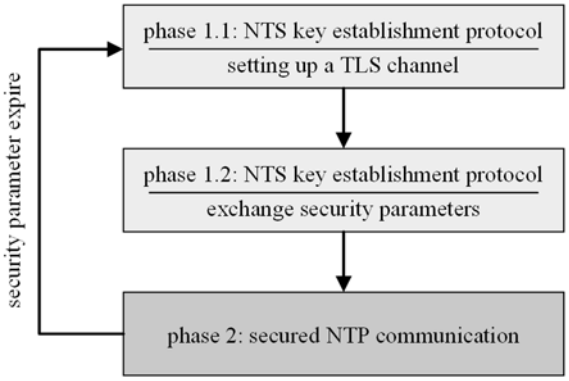

Fig. 3. Current schema of the NTS for NTP protocol.

4.2. Security in PTP

The security aspects of the Precision Time Protocol were also neglected for a long time. In the past there were some efforts to offer security functions, but these could never be established, so that until today the communication in PTP runs completely unsecured. Nowadays it has become obvious that, in addition to high synchronization accuracy, functioning protection mechanisms are also required, especially after NTS-for-NTP was published.

The first experimental attempts to secure PTP appeared in 2008 with Annex K described in IEEE Std. 1588-2008 [24]. This is a symmetric cryptography-based security mechanism that provides message integrity, group source authentication, and replay protection. The message integrity relies on a shared pre-shared key, although the key distribution is not addressed by the PTP standard. However, Annex K had no practical significance because no reference implementation was ever developed. One reason for this was that analyses in [25] [26] [27] revealed several design weaknesses. These include inefficient authentication procedures and algorithms, as well as insufficiently dimensioned sequence numbers for replay protection.

The evaluations were followed by proposals to improve the situation and include general design changes to Annex K [28]. These led to extensive changes to the security functions during the standardization work of PTPv2.1, so that the previous Annex K became obsolete and was finally replaced by a new Annex P [9]. Annex P describes the security

mechanisms in general terms, which are divided into so-called prongs. These are optional and can be used individually or in combination to protect messages in the PTP network.

4.2.1 Security Prongs of PTPv2.1

The current PTPv2.1 standard defines some security concepts that are divided into four prongs.

Prong A: This prong describes a built-in mechanism of PTP to ensure the authenticity and integrity of the PTPv2.1 messages. This mechanism consists of three components: key management, security processing method and AUTHENTICATION TLV. The protection mechanisms are distinguished into immediate security processing (ISP) and delayed security processing (DSP). With the immediate variant, the necessary security parameters and keys are transmitted upfront, before the secure PTP communication takes place. This allows all devices that know these parameters to immediately check incoming PTP messages. With the delayed variant, the key required for verifying the messages is disclosed by the master a posteriori. In general, the PTPv2.1 specification allows the use of both, manual and automatic key management systems. In a manual key management (KM) system, the security parameters are transferred to the PTP devices upfront and are usually static. While this is feasible for small PTP networks, it is not a solution for larger networks due to scaling issues. An automatic KM system solves these problems and enables a much better administration of the PTP network. However, PTPv2.1 does not define a specific key management system nor the associated communication or message structure.

Prong B: Another security strategy is the use of external mechanisms like MACsec [29] or IPsec [30]. Both approaches provide authenticity and message integrity and optionally allow the encryption of the higher protocol layers. MACsec works on layer 2 of the Open Systems Interconnection (OSI) model and is therefore restricted to peer-to-peer connections. IPsec works on layer 3 and allows tunnelling across networks, but due to the protocol stack, it cannot be used in conjunction with the 802.3 mode (Ethernet) in PTP.

Prong C: This prong provides guidance on how to protect a PTP network and provides solutions to mitigate DoS attacks by increasing the redundancy. This includes additional time sources and Grandmaster Clocks as well as redundant network paths.

Prong D: Another part is monitoring the network to detect attacks or problems in the infrastructure. This includes unexpected offset jumps or large changes in P2P measured PTP link delays.

4.2.2 Security Mechanisms and Protocols

At the present time, three security protocols for PTPv2.1 exist and are currently under development. This section gives a brief presentation of these solutions, which are described in more detail in [31].

NTS-for-PTP: Even before the release of the PTPv2.1 standard and the finalization of NTS as an RFC, we have already worked on an NTS-based security solution for PTP in early 2020 [32] [34] that is also the first realization of an automatic key management system for PTPv2.1. NTS-for-PTP (NTS4PTP) supports all transport and communication modes in PTP. For this purpose, it defines two approaches, both of which are based on the NTS protocol and implement the immediate security processing approach in PTP. The group-based approach (GrBA) focuses on multicast and mixed multicast/unicast connections, in which the key management server distributes group keys and controls the participants through authorization mechanisms. The ticket-based approach (TiBA), on the other hand, uses end-to-end connections that can be used to implement well-scalable unicast connections with high source authenticity. Both approaches also use a cyclic update mechanism that guarantees key freshness without interrupting a running PTP communication. NTS4PTP also uses TLSv1.3 as a phase-1 framework protocol and extends NTS in a way that allows the use of NTS-secured NTP and PTP with a common KM server. Furthermore, it specifies the previously missing communication path between key management server and the time server.

NTS for Negotiated Unicast PTP: After the submission of the NTS4PTP draft, the development of another NTS-based key management system focusing exclusively on the negotiated unicast mode in PTP (NTS4UPTP) started in early 2021 [34]. Due to the many years of development of NTS for NTP, its motivation is to provide protection for PTP as quickly as possible, with a focus on fending off amplification and replay attacks. Therefore, NTS4UPTP is designed to be as close as possible to NTS-for-NTP and provides a lightweight solution.

The protocol design focuses on a flow that is as similar as possible to NTS for NTP and therefore provides cookies for transporting keys and parameters. However, since some NTS goals such as statelessness of the time server and tracking protection are not necessary in the PTP context, some protocol parts have been simplified. NTS4UPTP also implements ISP in PTPv2.1 and uses symmetric keys to protect PTP messages. The authentication of the PTP instances is initially done via certificates and is solved during an active communication via a challenge-request-response procedure. Due to the E2E security, however, Transparent Clocks are not supported in unicast mode.

GDOI-for-PTP: The Group Domain of Interpretation (GDOI) protocol [35] is a proven standard designed for use with IPsec and is also used for multicast connections in field power-system automation. Therefore, work has also been started here since the end of 2020 to implement a GDOI-based key management system for PTP (GDOI4PTP) [31]. Due to the protocol, the focus lies on the formation of groups in which secured PTP multicast and mixed multicast/unicast connections are possible. However, group formation and authorization checking are not

part of the protocol and must be implemented manually or by external mechanisms. GDOI4PTP also implements the ISP approach in PTP and requires a phase-1 frame protocol for secure transmission of parameters and keys. The advantages of GDOI4PTP are that it supports Transparent Clocks and provides somewhat better group control capabilities. However, this approach only provides group authenticity and scales poorly when end-to-end-secured unicast connections are desired. Also, many protocol adaptations are necessary, as it is stated in [31, chapter 6].

5. Conclusions

In this paper, we have presented the current state-of-the-art regarding the security of time information and time protocols. Based on the Network Time Security protocol, NTP can already be effectively secured since 2020. However, this is somewhat restricted because NTS does not support all communication modes in NTPv4, nor does it specify the communication path between the key management server and the NTP time server. As for PTP, there are already three security protocols under development, two of which (NTS4PTP and GDOI4PTP) are actively in progress. Since no reference implementation is yet available for these protocols and PTP's built-in security solutions cannot be deployed out-of-the-box, there is currently no operational protection for PTP. However, due to active development, these will soon follow.

References

[1]. L. Levine, Metrologia, A review of time and frequency transfer methods, *IOP Publishing*, 2008, pp. 162-174.

[2]. D. L. Mills, J. Martin, J. Burbank, W. Kasch, Network Time Protocol Version 4: Protocol and Algorithms Specification, *Internet Engineering Task Force,* RFC 5905, 2010.

[3]. D. L. Mills, Network Time Protocol (NTP), *Internet Engineering Task Force,* RFC 958, 1985.

[4]. Network Time Foundation, NTPD (https://github.com/ntp-project/ntp).

[5]. E. Raymond, G. Miller, M. Selsky, H. Murray, NTPsec (https://gitlab.com/NTPsec/ntpsec).

[6]. M. Lichvar, V. Blut C. Christianson, Chrony (https://git.tuxfamily.org/chrony/chrony.git/).

[7]. B. Cook, OpenNTPD (https://github.com/openntpd-portable).

[8]. IEEE Standard for a Precision Clock Synchronization Protocol for Networked Measurement and Control Systems, *IEEE Std 1588-2002*, 2002.

[9]. IEEE Standard for a Precision Clock Synchronization Protocol for Networked Measurement and Control Systems, *IEEE Std 1588-2019*, 2020.

[10]. The Linux PTP Project (https://www.linuxptp.org/)

[11]. PTP daemon PTPd (https://github.com/ptpd/ptpd)

[12]. A. Malhotra. I. Cohen, E. Brakke, S. Goldberg, Attacking the Network Time Protocol, *Cryptology ePrint Archive*, 2015, Paper 2015/1020.

[13]. T. Mizrahi, Security Requirements of Time Protocols in Packet Switched Networks, *Internet Engineering Task Force,* RFC 7384, 2011.

[14]. P. V. Estrela, S. Neusüß, W. Owczarek, Using a multi-source NTP watchdog to increase the robustness of PTPv2 in financial industry networks, in *Proceedings of the IEEE International Symposium on Precision Clock Synchronization for Measurement, Control, and Communication (ISPCS '2014)* , 2014, pp. 87-92.

[15]. B. Moussa, M. Debbabi, C. Assi, A Detection and Mitigation Model for PTP Delay Attack in an IEC 61850 Substation, *IEEE Transactions on Smart Grid*, Vol. 9, No. 5, 2018, pp. 3954-3965.

[16]. F. Anwar et al., Timeline: An Operating System Abstraction for Time-Aware Applications, in *Proceedings of the IEEE Real-Time Systems Symposium (RTSS '2016)* , 2016, pp. 191-202.

[17]. D. L. Mills, Network Time Protocol (Version 3) Specification, Implementation and Analysis, *Internet Engineering Task Force,* RFC 1305, 1992.

[18]. D. L. Mills, U. Delaware, B. Haberman, Network Time Protocol Version 4: Autokey Specification, *Internet Engineering Task Force,* RFC 5906, 2010.

[19]. S. Röttger, Analysis of the NTP Autokey Procedures, Project Thesis, *Technische Universität Braunschweig*, Institute of Theoretical Computer Science, 2012.

[20]. D. Sibold, S. Röttger, Network Time Protocol: autokey Version 2 Specification, *Internet Engineering Task Force*, Internet-Draft, draft-sibold-autokey-02, 2013.

[21]. D. Franke, D. Sibold, K. Teichel, M. Dansarie, R. Sundblad, Network Time Security for the Network Time Protocol, *Internet Engineering Task Force*, RFC 8915, 2020.

[22]. E. Rescorla, The Transport Layer Security (TLS) Protocol Version 1.3, *Internet Engineering Task Force*, RFC 8446, 2018.

[23]. M. Langer, et al., NTP-O: first NTS capable NTP implementation (https://gitlab:com/MLanger/ntp)

[24]. IEEE Standard for a Precision Clock Synchronization Protocol for Networked Measurement and Control Systems, *IEEE Std 1588-2008* (Revision of IEEE Std 1588-2002), 2008.

[25]. E. Itkin, A. Wool, A Security Analysis and Revised Security Extension for the Precision Time Protocol, *IEEE Transactions on Dependable and Secure Computing*, Vol. 17, No. 1, 2020, pp. 22-34.

[26]. C. Önal, H. Kirrmann, Security improvements for IEEE 1588 Annex K: Implementation and comparison of authentication codes, in *Proceedings of the IEEE International Symposium on Precision Clock Synchronization for Measurement, Control and Communication*, 2012, pp. 1 - 6.

[27]. B. Hirschler, A. Treytl, Validation and verification of IEEE 1588 Annex K, in *Proceedings of the IEEE International Symposium on Precision Clock Synchronization for Measurement, Control and Communication*, 2011, pp. 44 - 49.

[28]. N. Moreira, J. Lázaro, J. Jimenez, M. Idirin, A. Astarloa, Security mechanisms to protect IEEE 1588 synchronization: State of the art and trends, in *Proceedings of the IEEE International Symposium on Precision Clock Synchronization for Measurement, Control, and Communication (ISPCS '2015)*, 2015, pp. 115 - 120.

[29]. IEEE Standards Association, IEEE Standard for Local and metropolitan area networks-Media Access Control (MAC) Security, *IEEE Std 802.1AE-2018* (Revision of IEEE Std 802.1AE-2006), 2018.

[30]. K. Seo, S. Kent, Security Architecture for the Internet Protocol, *Internet Engineering Task Force*, RFC 4301, 2005.

[31]. M. Langer, S. Fries, M. Rohde, K. Heine, D. Sibold, R. Bermbach, PTP Security Key Management Solutions, in *Proceedings of the IEEE International Symposium on Precision Clock Synchronization for Measurement, Control, and Communication (ISPCS '2021)*, 2021, pp. 1-6.

[32]. M. Langer, R. Bermbach, NTS4PTP - Key Management System for the Precision Time Protocol Based on the Network Time Security Protocol, *Internet Engineering Task Force*, Internet-Draft, draft-langer-ntp-nts-for-ptp-04, 2022.

[33]. M. Langer, R. Bermbach, NTS4PTP - A comprehensive key management solution for PTP networks, *ELSEVIER Computer Networks*, Vol. 213, 2022, 109075.

[34]. H. Gerstung, M. Rohde, D. Arnold, Network Time Security for the Unicast Mode of the Precision Time Protocol, *Internet Engineering Task Force*, Internet-Draft, draft-gerstung-nts4uptp-03, 2021.

[35]. T. Hardjono, S. Rowles, B. Weis, The Group Domain of Interpretation, *Internet Engineering Task Force*, RFC 6407, 2011.

(009)

Design of Low Phase Noise 100 MHz VCXO with Wide Frequency Pulling Range

Songtao Jiang [1], Haijun Wu [1], Changming Dai [1], Kaizhong Zhan [1], Lin Xu [2] and Feng Tan [2]
[1] Chengdu Spaceon Electronics Co., Ltd. No.66 Sheng Ye Road, Jin Niu District, Chengdu City, Si Chuan Province, China
[2] University of Electronic Science and Technology of China, School of Automation Engineering, Qingshuihe Campus: No.2006, Xiyuan Ave, West Hi-Tech Zone, 611731, Chengdu, China
Tel.: + 86 02861831304
E-mail: tanfeng@uestc.edu.cn

Summary: Due to its characteristics of electrically tunable frequency, VCXO is widely used in many fields such as Electrical calibration, PLL, TCXO, frequency modulation and Frequency agility technology. The design of low phase noise VCXO with wide frequency pulling range is still a challenge. In this work, on the basis of theory of quartz crystal resonator and phase noise of Leeson model, combined with ADS simulation analysis, the correlation between the frequency pulling range of VCXO and its phase noise is studied. The sample of 100 MHz VCXO with the pulling range of ±25 ppm and the phase noise of ≤-158 dBc/Hz @ 1 kHz, ≤-172 dBc/Hz @ 10 kHz is accomplished. Experimental result shows that, by adjusting the relevant parameters of the crystal resonator and selecting the varactor with large varactor ratio, the VCXO with large frequency pulling range and low phase noise can be obtained.

Keywords: Quartz crystal resonator, VCXO, Phase Noise, electrically tunable frequency, Frequency pulling range.

1. Introduction

Quartz crystal oscillator, often regard as the "heart" in electronic systems, is widely used in many electronic systems. In fact, as an important type of oscillator, voltage controlled crystal oscillator(VCXO) is widely used in many fields such as electrical calibration, PLL, TCXO, frequency modulation, tame system, base stations and optical communication systems, because of the characteristics of electrically tunable frequency[1].

The main specifications of VCXO are the frequency pulling range and the phase noise. Previous researchers have studied VCXO from multiple perspectives, including crystal resonators, phase noise model and circuits [2]. Y. Takahashi reported a circuit architecture of integrated circuits (ICs) applied to the development of a high performance voltage controlled crystal oscillator (VCXO) [3]. Ulrich L. Rohde reported a novel approach for optimizes the start-up characteristics and drive sensitivity factor for achieving high performance VCXO [4]. Yao Huang Kao [5] described their investigation using CMOS varactors.

In this paper, the main factor of the frequency pulling range is studied, and the relation between the phase noise and the frequency shift is also derived.

2. Theory

2.1. Frequency Pulling Characteristics of Crystal Resonator

As we know, the equivalent circuit of a resonator was modeled by BVD circuit, the crystal resonator has two resonant frequencies. One is the series resonant frequency f_s. Another is the parallel frequency f_p.

The relative series and parallel frequency interval of the crystal resonator can be obtained as below.

$$\frac{\Delta f}{f_s} = \frac{f_p - f_s}{f_s} \approx \frac{C_q}{2C_0} \tag{1}$$

where f_s is series resonant frequency; f_p is parallel resonant frequency.

The frequency of the crystal resonator can be adjusted by series a varactor or a capacitor (C_L), and the frequency shift can be expressed:

$$\frac{\Delta f_L}{f_s} = \frac{C_q}{2\left(C_0 + C_L\right)} \tag{2}$$

The maximum frequency shift is determined by Eq. (1). Obviously, in order to increase the frequency pulling range of high frequency overtone crystal, it is necessary to reduce the static capacitance C_0 of crystal resonator.

2.2. Relationship between Phase Noise and Frequency Shift

As it is shown in Eq. (5), when the capacitance of the series varactor is changed ΔC_L, the relative frequency shift can be given:

$$\Delta\left(\frac{\Delta f}{f_s}\right) = -\frac{C_q}{2\left(C_0 + C_L\right)}\Delta C_L \tag{3}$$

For Pierce oscillator circuit, the Q_L of its resonant tank is given in Ref[6].For small change of C_L, explicit expression is described in Eq.(4).

$$\Delta Q_L = \frac{2QC_0}{(1+C_0/C_L)^3 C_L^2}\Delta C_L \qquad (4)$$

Moreover, according to phase noise of Leeson model [7], the change of oscillator's phase noise which caused by the change of Q_L can be expressed as below.

$$\Delta L(f_m) = \frac{1}{2}\frac{FkT}{P_{si}}(1+\frac{f_c}{f_m})(1-\frac{f_0^2}{4f_m^2Q_L^3})\Delta Q_L \qquad (5)$$

And thus, one can find that the phase noise will vary with the value of the capacitance of the varactor.

3. Figures and Tables

In this work, the 3rd overtones, AT-cut 100MHz surface mountable resonator packaged in 5032 is used (KDK Co. Ltd), and the Parameters of the 100 MHz resonator is shown in Table 1. The Parameters of the 100MHz resonator is measured by S&A250B-1 (SAUNDERS Co. Ltd).

Fig. 1 shows the influence of the static capacitance C_0 on the series and parallel frequency interval of the crystal resonator. The static capacitance C_0 varies from 1.0 pF to 1.9 pF. One can see that the smaller the static capacitance, the larger frequency interval. And the larger frequency interval, the larger pulling ratio. It is well agree with the Eq. (1).

Table 1. Parameters of the 100MHz resonator.

No.	R, (Ω)	L, (mH)	C_0,(pF)	C_1,(fF)	Q,(k)
1.	35.8	4.7	1.7	0.5	82

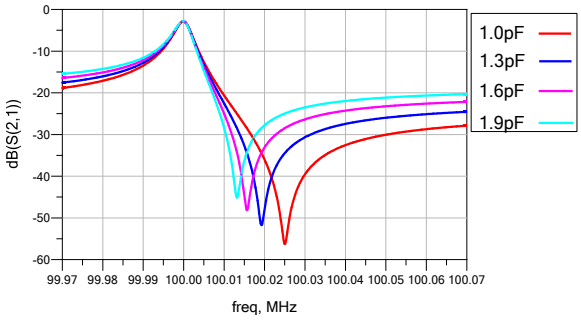

Fig. 1. The relation between the static capacitance and frequency interval of the resonator

In this work, the Pierce oscillator circuit is used. The frequency pulling range is about ±25 ppm.

Fig. 2 shows the phase noise of the sample of VCXO, The measured phase noise is better than -158 dBc/Hz @ 1 kHz and -172 dBc/Hz @ 10 kHz (FSWP8, R&S Co. Ltd).

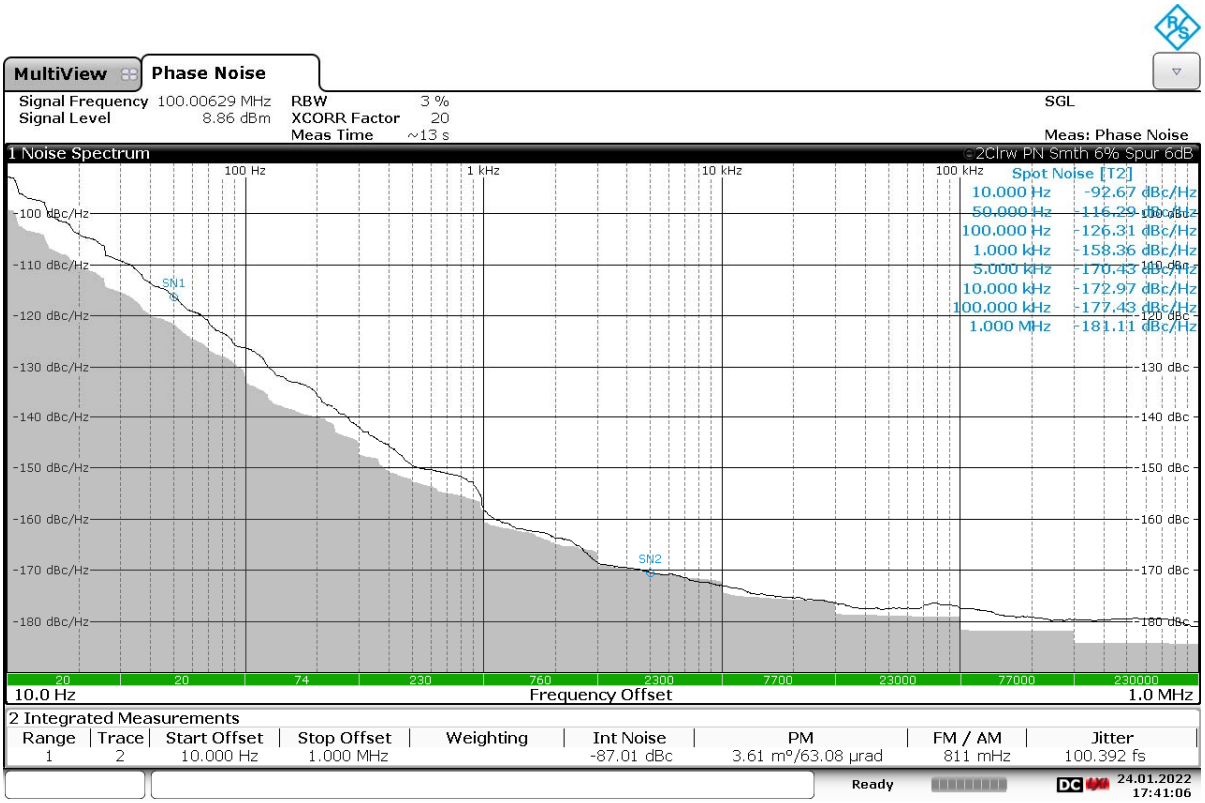

Fig. 2. The phase noise plot of 100MHz VCXO.

4. Conclusions

Large pulling frequency range and low phase noise VCXO is studied. It is benefit to expand the frequency pulling range by reducing static capacitance. Moreover, it is also found that the higher of Q_L, the lower of phase noise.

Acknowledgements

This work was supported the National Natural Science Foundation of China (Grant No. 61701077) and the Fundamental Research Funds for the Central Universities (Grant No. ZYGX2019J056).

References

[1]. Helle, J., VCXO Theory and Practice, in *Proceedings of the 29th IEEE Symposium on Frequency Control*, 1975, pp. 300 - 307.

[2]. R. I. Ruslan, T. Satoh, T. Akitsu, Voltage-Controlled Narrowband and Wide Variable -Range Four-Segment Quartz Crystal Oscillator, *IEEE Trans. Ultrason. Ferroelectr. Freq. Control*, Vol. 59, March 2012, pp. 564-572.

[3]. Takahashi, Y., et al., A low noise, wide variable range and high linearity VCXO-IC using linearity designable on-chip varactor arrays for fundamental AT-cut crystal resonators, in *Proceedings of the IEEE International Frequency Control Symposium*, 2014, pp. 1-6.

[4]. Rohde, U. L., and A. K. Poddar, Noise minimization techniques for voltage controlled crystal oscillator (VCXO) circuits, in *Proceedings of the IEEE Radio and Wireless Symposium (RWS '09)*, 2009, pp. 280 - 283.

[5]. Yao, H. K., and T. C. Liau, Study of phase noise in VCXO with inversion-mode varactors, in *Proceedings of the IEEE European Frequency & Time Forum & International Frequency Control Symposium*, 2014, pp. 149 - 152.

[6]. Xianhe Huang, Yan Wang, Wei Fu, et al., The design and implementation of a 120-MHz Pierce low-phase-noise crystal oscillator, *Trans. Ultrason. Ferroelectr. Freq. Control*, 58, 7, 2011, pp. 1302-1306.

[7]. D. B. Leeson, A Simple Model of Feedback Oscillator Noise Spectrum, *Proceedings of the IEEE*, 54, 1966, pp. 329-330.

(011)

Radio Wave Underground Sounding by the SDI K-5 Radar for Obtaining 3D Topographic Images of Geological Structures

A. M. Kudelya [1], Yuriy Vashpanov [2], Jung-Young Son [3] and Tatyana Podousova [4]
[1] Faculty automation and information technologies, Kiev National University of Civil Engineering and Architecture, Kiev, 03037, Ukraine
[2] Department of Physics, Odessa State Academy of Civil Engineering and Architecture, Odessa, 65029, Ukraine
[3] Department of Civil Engineering, Konyang University, Nonsan, Chungnam, 32992, Republic of Korea
[4] Department of Applied Mathematics, Odessa State Academy of Civil Engineering and Architecture, Odessa, 65029, Ukraine
E-mail: vashpanov@hanyang.ac.kr or yuriy.vashpanov@gmail.com

Summary: Radio wave responses from the underground structure of a concrete dam were experimentally studied using ground penetrating radar. The developed SDI K-5 in the frequency range of 1-10 MHz for geophysical research consists of small inductive loops less than 1 meter long. Two components of the electromagnetic field were measured: the vertical magnetic Hz and electric Ex components, the sum of these components, and the differential phase shift. The obtained experimental data were processed in the OriginLab program by special mathematical transformations. Computer processing of experimental data made it possible to obtain a 3D image of the cavity inside the dam, which is not visible to a person from the surface. The 3D dimensions of this cavity under the concrete surface can be measured with an accuracy of 5 %. The method can be applied to detect hidden areas of concrete structures.

Keywords: Frequency, Phase, Radio wave sounding, Ground penetration radar, Geometrical topology.

1. Introduction

The technology of radio-wave method (RWM) allows survey of ground areas in terms of determination of their lithological structure by genesis, detection of horizons filtration flows of the ground waters, the minerals deposit search and, etc. [1-3]. RWM is one of geophysical research techniques which are based on study of the process of electromagnetic waves propagation through rocks and observation of inductive effects in ground layers with different values of conductivity, dielectric permittivity and magnetic permeability. Among RM methods one may distinguish a separate group of inductive methods in which the electromagnetic field is created by of the loop with the variable current. As loops one may use small-size frames, large rectangular loops, very long cables, etc. [4, 5].

We are developing an inductive method, the idea of which is as follows. The primary alternating field of the loop induces eddy currents in the conducting geoelectric section, the intensity of which is determined by the resistivity of the geoelectric section and its magnetic properties, as well as the position of the loop. Currents flowing on subsurface of media create secondary magnetic field which overlaps over the primary magnetic field and creates abnormalities (responses to influence of the first magnetic field) which to measure with the help of receiving loop.

If place two small-size loops on the ground surface, and name one of them generator magnetic dipole which generates the first variable electromagnetic field, and the second one – the measuring magnetic dipole, then two such loops may compose a dipole inductive radio- wave system, which may be used for profiling and sounding of ground massif. Dipole inductive profiling (DIP) is performed without any changes in mutual position of the loops.

2. Experiments using the Ground Penetrating Radar SDI K-5.

A radio wave transmitter (T) located at the surface issued to generate radio waves which penetrate into the subsurface. Some of the energy carried by these waves is transmitted to greater and greater depths, while some of the energy is reflected back towards the surface receiver (R) whenever a contrast in dielectric properties is encountered. The amount of energy reflected is dependent on the contrast in electrical properties encountered by the radio waves.

Physically difficult to use a GPR-type high-frequency georadar for the following reasons. GPR sounding of wet soils requires a frequency range of the order of (100 400) MHz and a flat ground surface. In this frequency range, antenna systems have dimensions of the order of 1 m^2.

Our method is based on the study of the process of propagation of electromagnetic waves in rocks and the observation of induction effects in soil layers with different values of conductivity, dielectric and magnetic permeability. In inductive methods, an electromagnetic field is created using ungrounded circuits (frames) flowed around with alternating current. Two frames (generator magnetic dipole and receiving magnetic dipole) make up a dipole inductive system (DIS) for profiling and probing the soil mass.

The sounding depth is determined by the distance between the transmitter and receiver antenna systems, [6]. Dipole inductive profiling (DIP) is performed without changing the relative position between the frames. By changing the distance between the frames, dipole inductive sounding (DIS) is performed, which is commonly called geometric. To perform DIZ and DIP, equipment was used - a dipole inductive structuroscope SDI K 5 [7] (Fig. 1. Ground Penetrating Radar SDI K-5 on the dam at Nonsun, Republic of Korea). In the case of placing the generator and receiving antenna systems in the hollow space of the rock mass (tunnel), the sounding depth is determined by half the base between the antennas.

Fig. 1. Ground Penetrating Radar SDI K-5 on the dam at Nonsun, Republic of Korea. **T** is the radio wave transmitter, **R** is the receiver.

Changes of distance between the loops carry out dipole inductive sounding (DIS) which is usually called geometric. One of modification of inductive methods and equipment for geophysical survey of structure rocks is DIRS, which is named Ground Penetrating Radar, SDI K-5. The georadar by radio-wave method sounding of rocks in a geometrical version. The georadar SDI K-5 consists of the crossed magnetic dipoles: generating and reception, located on the theodolites' tripods.

As a rule, in the standard measuring equipment for performance of geophysical researches by some inductive method measurements of one - two data of an electromagnetic field are carried out. Loops of the big sizes for search geology are thus used. And it is natural, that such equipment has the spatial resolution of an order of one – tens meters. Developed SDI K-5 for performance of geophysical researches consists of small inductive loops less than 1 meter in the frequency range of 1 10 MHz.

For increase of probability of identification of soil layers on seeming specific resistance or definitions of their condition in time, SDI K-5 to measures two components of an electromagnetic field: vertical magnetic Hz and electrical Ex components, the sum, of these a component and differential phase shift, ($\Delta\ \varphi$), between them. These data register in electronic memory of a SD card and further are transferred to the computer for the further calculations. All procedures of data gathering and their processing can be automatically carry out on in advance chosen algorithm.

Compactness of dipole inductive system and its resistance to external electromagnetic effects give the possibility to perform geophysical survey under various conditions of ground and water surface, vegetation and weather.

The standard tomographic image of a vertical geophysical cut on 2 real points of and 1 virtual point of sounding obtain from calculation is executed on the sum Hz and Ex shows on Fig. 2.

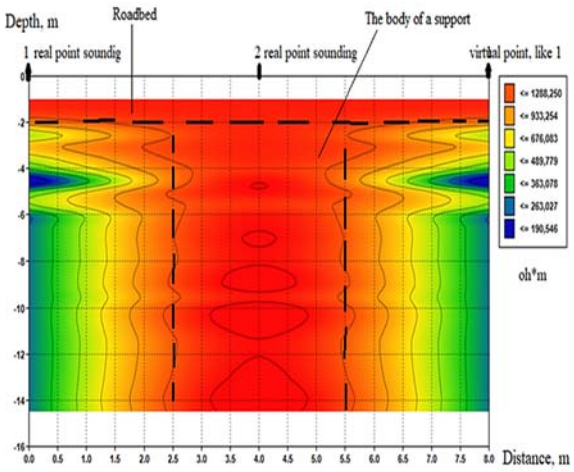

Fig. 2. The tomographic image of a vertical geophysical cut on 2 real points of and 1 virtual point of sounding obtain from calculation is executed on the sum Hz and Ex, where is:
1 point - is real point sounding on depth 6m and located between supports of the bridge of a dike dam.
2 point - is real point sounding on depth 14.5 m and located under middle of support of the bridge of a dike dam.
3 point - is virtual point sounding on depth 6m and located between supports of the bridge of a dike dam.

3. Computer Processing of Radio Sounding Data for Ground-Penetrating Radar SDI K-5 for 3D Graph Analyses of Ground Surfaces Geological Properties

Practical application of Ground-Penetrating Radar technology demand on analyses geological properties of topology ground surfaces. We used a computer method for the convert experimental data to a 3D surface graph, which published in our paper [8-10]. Experimental data of radio sounding using of the Ground-Penetrating Radar SDI K-5 was written in the

ASCII table by microcontroller and then imported to OriginLab program. Where *x, y* are coordinates of measurement points, Hz and Ex are magnitudes of magnetics and electrical fields, φ is an angle between vectors Hz and Ex, S is a total magnitude of signal. A total number of our measurements is 50. A fragment of experimental data of radio wave sounding using of the Ground-Penetrating Radar SDI K-5 for the dam surface area 50×25 m2 is presented on the Table 1. 3D graphs and surface topographies for the Hz, Ex and φ data of the geological object are shown in Figs. 3-8.

Table 1. Fragment of experimental data of radio sounding using of the Ground-Penetrating Radar SDI K-5 for the dam surface area 50×25 m^2.

Log name	*x*	*y*	*Hz*	*Ex*	ϕ	*S*
Units	m	m		V/m	rad	
1	0	0	1.0032	1.8675	1.5534	0.926
2	5	0	1.0678	1.7884	1.1227	0.8772
3	10	0	0.6888	1.6872	0.6687	0.9801
4	15	0	0.7091	1.2947	0.3902	0.8262
5	20	0	1.3565	1.3364	0.0931	0.6229
6	25	0	0.9716	1.4912	0.6306	0.8079
…..						
43	10	25	0.3465	1.2473	0.7337	0.9779
44	15	25	0.517	1.2964	1.0758	0.9186
45	20	25	0.6804	1.3987	1.2557	0.8883
46	25	25	0.6496	1.3525	1.2318	0.8849
47	30	25	0.6541	1.4113	0.9908	0.8978
48	35	25	0.9982	1.3896	1.0391	0.7698
49	40	25	1.0584	1.4437	1.0733	0.7657
50	45	25	0.8704	1.4319	1.0093	0.8291

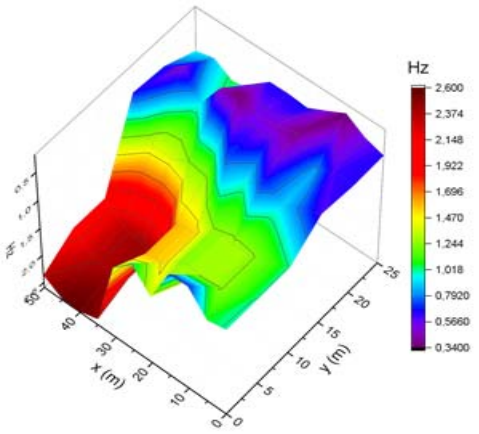

Fig. 3. 3D graph for the *Hz* data of the geological object (the dam at Nonsun, Republic of Korea).)

The radio wave method was used to study the area of the dam surface with a size of 25x50 m^2 to a depth of 50 m. Based on the results of processing the received field data of the components of the electromagnetic field, the vertical magnetic component Hz, the electrical Ex, the phase shift Δφ between Hz and Ex, and the vector sum of the components Hz and Ex, 3D images of the sections of the studied rock mass were constructed. Fig. 4 shows a 3D vertical geological and geophysical section of the rock mass to a depth of 50 m. The color scheme on the scale shows the parameters of rocks in terms of apparent electrical resistivity in ohm. According to the obtained parameters of rocks from the surface to a depth of 50 m, the following interpretation of the 3D image is possible: up to depths of about 10 m, the rock mass is composed of soft soils with a resistivity of 300 to 700 ohm. With an increase in depth to 50 m, a crystalline fault with a resistivity of about 2600 Ohm×m is observed in the coordinates *x* (45÷50) m and *y* (0±15) m.

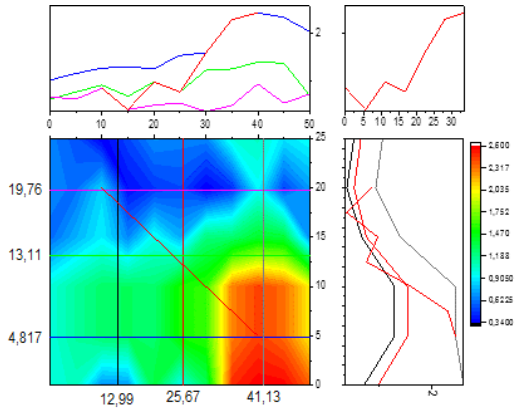

Fig. 4. Surface topography of this geological object.

Figs. 3 and 4 give the spatial arrangement of the cavity in the concrete structure of the dam. The cavity under the concrete surface can be measured with an accuracy of 5 %.

Figs. 5 and 6 describe the response of the Ex parameter for the investigated geological structure.

3D graphs for parameters φ and S (Figs. 7 and 8) differ from the previous ones. A deep theoretical analysis of these results is required, which may be the subject of the following studies.

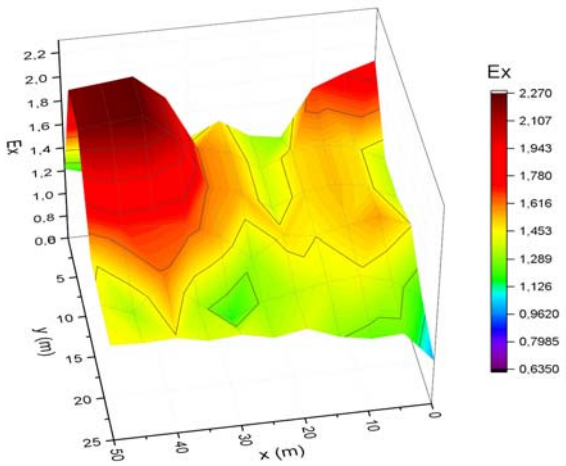

Fig. 5. 3D graph for the Ex data of our geological object.

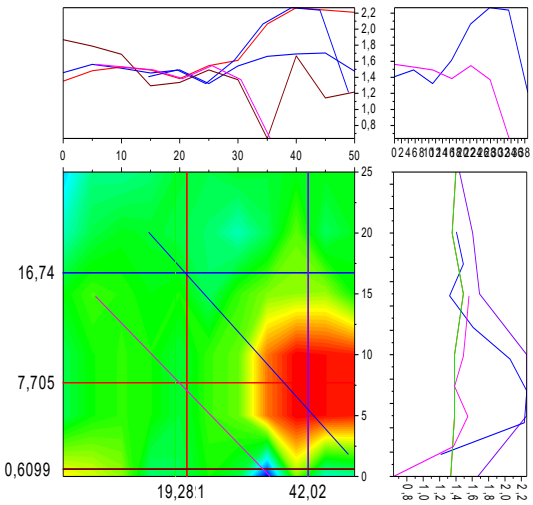

Fig. 6. Surface topography for the Ex data of our geological object.

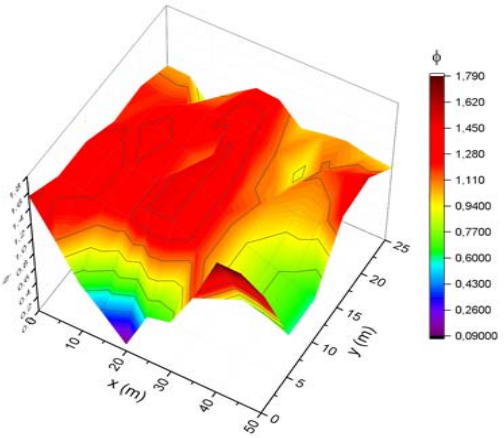

Fig. 7. 3D graph of the phase distribution under the dam surface.

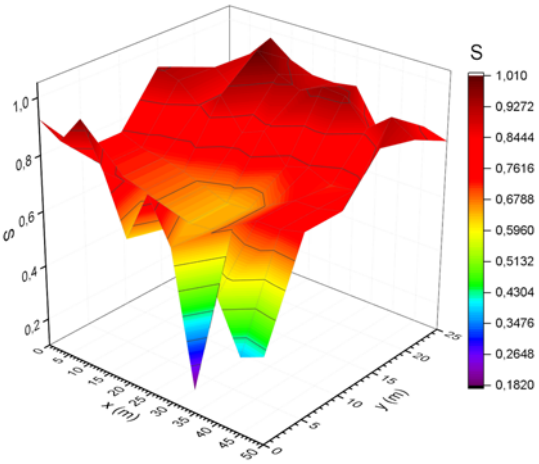

Fig. 8. 3D graph for the parameter S distribution under the dam surface.

4. Conclusions

Our studies performed by the radio wave method based on the impulse Ground-Penetrating Radar SDI K-5 showed the possibility of:

1) Measurements of the topology of the internal structure of the concrete structure of the dam in the form of a longitudinal vertical section;

2) The use of computer processing of experimental data made it possible to obtain a 3D image of the cavity inside the dam, not visible to humans from the surface.

References

[1]. M. S. Zhdanov, Foundations of geophysical electromagnetic theory and methods, Second Edition, *Elsevier,* 2018.

[2]. M. S. Zhdanov, Geophysical technique for mineral exploration and discrimination based on electromagnetic methods and associated systems, *US Patent 7,324,899 B2*, 2008.

[3]. M. S. Zhdanov and G. V. Keller, The geoelectrical methods in geophysical exploration, *Elsevier*, 2009.

[4]. B. S. Svetov, Theory, methodology and interpretation of materials of low-frequency inductive electro-investigation, *Nadra*, Moskow, (in Russian), 1973.

[5]. V. K. Hmelevskoj, B. P. Petruhin, P. J. Pushkarev Magnito-tellurika and radiowave inter-ferentsionnye sounding, *Physics of the Earth, Geological faculty of the Moscow State University of Lomonosov*, 2010, 9, pp. 9-14.

[6]. A. M. Kudelya, Evaluation of radio wave method (RM), sounding the soil mass, *Geophysical Journal*, 2014, Vol. 36, 1, pp. 170–176.

[7] A. M. Kudelya, Radiowave Structuroscope RS-01, *Patents of Ukraine: No. 102848, No. 102846, No. 102887, No. 02836,* Kiev, Ukraine.

[8]. Yuriy Vashpanov, Jung-Young Son, Gwanghee Heo, Tatyana Podousova and Yong Suk Kim Vision-based Measurement of Geometric Parameters of Cracks in Concrete, in Anuj Kumar Goel (Ed.), Advanced Aspects of Engineering Research, Vol. 11, *BP International,* London, Chapter 5, 2021, pp. 41-58.

[9]. Yuriy Vashpanov, Jung-Young Son, Gwanghee Heo, Tatyana Podousova, and Yong Suk Kim,

Determination of Geometric Parameters of Cracks in Concrete by Image Processing, *Advances in Civil Engineering,* 2019, Article ID 2398124.

[10]. Yuriy Vashpanov, Gwanghee Heo, Jung-Young Son and Tatyana Podousova, Remote optical measurements of cracks in concrete structures using computer image processing, *IOP Conf. Series: Materials Science and Engineering,* 1141, 2021, 012028.

(010)

Dependence of Acousto-Optical Properties of $PbMoO_4$ Crystals on Direction of Wave Vector of Acoustic Waves

F. R. Akhmedzhanov, M. I. Elboeva and S. Z. Mirzaev
Institute of Ion-Plasma and Laser Technoligies, UFO Laboratory,
33 Durmon yuli str., 100125 Tashkent, Uzbekistan
Tel.: + 998902121998, fax: + 998712623254
E-mail: akhmedzhanov.f@gmail.com

Summary: The dependence of the acousto-optic properties of lead molybdate crystals on the direction of the wave vector of longitudinal acoustic waves in the symmetry plane has been studied. The photoelastic constants were determined by the Dixon method in the mode of Bragg light-by-sound diffraction. The geometries of light diffraction are determined, which make it possible to obtain the maximum values of the acousto-optical quality. It is shown for the first time that it is possible to control the efficiency of Bragg light diffraction by changing the direction of the wave vector of an acoustic wave.

Keywords: Acoustic wave, Polarization, Acousto-optic quality factor, Bragg light diffraction, Lead molybdate crystals, Acoustic wave velocity.

1. Introduction

It is known that lead molybdate crystals are widely used in various acousto-optic devices [1–5]. Of particular interest are methods for controlling the intensity of diffracted light when these crystals are used as an active acoustic medium [6, 7]. In this work, the dependence of the effective photoelastic constant peff and the acousto-optic quality factor M_2 on the direction of propagation of longitudinal acoustic waves in the (001) crystallographic plane has been studied. The obtained results make it possible to reveal the most optimal geometries of Bragg light diffraction with the highest efficiency.

2. Samples and Experimental Methods

The PbMoO4 samples were oriented along the [100] [010] and [001] crystallographic axes with an accuracy of one degree. The measurements were carried out at room temperature by the method of Bragg light diffraction by acoustic waves with frequencies of 400–1200 MHz, which were excited by X-cut quartz piezoelectric transducers [8]. The light source was a helium-neon laser (λ_0 = 632.8 nm). The direction of polarization of the light beam incident on the sample relative to the wave vector and polarization of the acoustic wave was determined using a polarization analyzer.

The effective photoelastic constants, and then the components of the photoelasticity tensor, were determined by the modified Dixon-Cohen method [9]. The acoustic wave velocities along the [100] and [001] axes required for the calculation were determined from the angle of Bragg light diffraction on these waves with an accuracy of 0.2 % [8].

3. Results and Discussion

Based on the measured values of the intensities of diffracted light for different directions and polarizations of light and acoustic waves, the effective photoelastic constants peff in lead molybdate crystals were determined. Then, using the experimental values of the velocity of acoustic waves and the data on density and refractive indices from [6], the coefficients of the acousto-optic quality M2 were calculated.

The results for the main crystallographic directions in lead molybdate crystals are presented in Table 1. In the table vectors **q** and **γ** indicate, respectively, the direction of the wave vector and the polarization of acoustic waves in lead molybdate crystals.

It should be noted that the calculated values of the coefficient M_2 agree well with its experimental values available in the literature for the [100] and [001] directions [2, 3]. The components of the polarization vector and the orientation angle of this vector relative to the [100] axis in the (001) plane were determined from the relationship:

Table 1. Velocity of acoustic waves, effective photoelastic constants, and acousto-optic quality factor in $PbMoO_4$ crystals.

q	**γ**	V, 10^3m/s	P_{eff}	M_2, $10^{-15}s^3/kg$
[100]	[100]	3.78	p_{11}=0.240	24.1
	[001]	2.46	p_{44}=0.067	6.82
[001]	[001]	4.01	p_{33}=0.296	30.7
	[100]	2.12	p_{44}=0.067	10.6
[010]	[010]	3.78	p_{11}=0.240	28.3
	[001]	2.46	p_{44}=0.067	6.82
[110]	[110]	4.23	$p_{11}+p_{66}$=0.3	25.1
	[001]	1.64	p_{61}=0.013	7.29

$$\psi = arctg\frac{\gamma_2}{\gamma_1} = arctg\left(\frac{\rho V^2 - \Gamma_{11}}{\Gamma_{12}}\right) \qquad (1)$$

The following values of elastic constants were used in the calculation: c_{11} = 1.36 × 10^{10} N/m^2, c_{33} = 9.17 × 10^{10} N/m^2, c_{44} = 2.67 × 10^{10} N/m^2, c_{66} = 3.37 × 10^{10} N/m^2. Additional quantities required for the calculation were taken from [3]. These results are shown in Figure 3 as a deviation of the polarization vector from the direction of the wave vector.

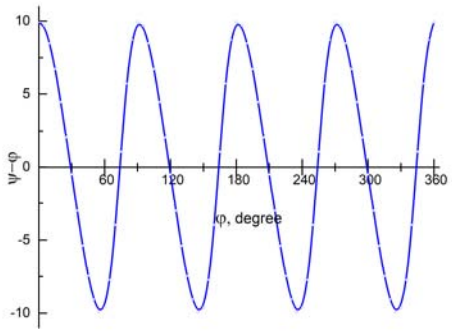

Fig. 1. Deviation of the polarization of longitudinal acoustic waves from the direction of the wave vector in the (001) plane in $PbMoO_4$.

The dependence of the acousto-optic quality factor on the direction of the wave vector of longitudinal acoustic waves in the (001) plane is shown in Fig. 2.

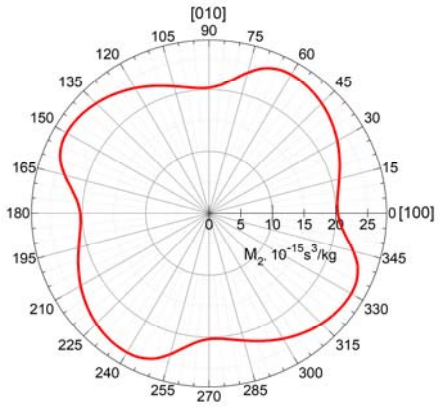

Fig. 2. Dependence of the M2 coefficient on the direction of the wave vector of quasi-longitudinal acoustic waves in $PbMoO_4$ crystals in the (001) plane.

It can be seen that the highest value of the acousto-optic quality factor is observed for longitudinal acoustic waves propagating in the (001) plane at angles of 60 and 150 degrees to the [100] axis.

4. Conclusions

The anisotropy of the acousto-optic interaction in $PbMoO_4$ crystals is studied for the first time when the direction of propagation of longitudinal acoustic waves in the (001) plane is changed. It is shown that for longitudinal waves in the (001) plane there are four directions, which are longitudinal normals, along which the pure longitudinal acoustic waves propagate.

The acousto-optical quality factor for the diffraction of light by these pure longitudinal acoustic waves is 25 10^{-15} s^3/kg and it is close to the maximum value of the coefficient M_2 for the considered Bragg light diffraction geometries.

References

[1]. S. T. Narasimhamurthy. Photoelastic and electro-optical properties of crystals, *Mir*, Moscow, 1984.

[2]. E. Dieulesaint, D. Royer, Elastic waves in solids. Application for treatment of signals, *Nauka*, Moscow, 1982.

[3]. Acoustic crystals. Handbook, Ed. M.P. Shaskolskaya, *Nauka*, Moscow, 1982.

[4]. Erba, R. Dovesi, Photoelasticity of crystals from theoretical simulations, *Phys. Rev.*, Vol. B88, 2013, pp. 045121.

[5]. V. T. Gabrielyan, V. V. Kludzin, S. V. Kulakov, B. P. Razzhivin, Elastic and photoelastic properties of lead molibdate monocrystals, *Solid State Phys.*, Vol. 17, 1975, pp. 603-605.

[6]. G. A. Coquin, D. A. Pinnow, A. W. Warner, Physical properties of lead molybdate relevant to acustooptic device applications, *Appl. Phys.*, Vol. 42, 1971, pp. 2162-2168.

[7]. F. R. Akhmedzhanov, Application of acoustical activity for measurement of acoustic wave frequency, in *Proceedings of the Frequency Control Symposium, joint with the 22nd European Frequency & Time Forum*, Besancon, France, 2009, pp. 613-615.

[8]. F. R. Akhmedzhanov, J. O. Kurbanov, A. F. Boltabaev, Attenuation of Acoustic Waves in Single-domain and Polydomain LiTaO3 Crystals, *Sensors & Transducers*, Vol. 246, Issue 7, 2020, pp. 43-47.

[9]. R. W. Dixon, M. G. Cohen, A New Technique for Measuring Magnitudes of Photoelastic Tensors and its Application to Lithium Niobate, *Appl. Phys. Letter*, Vol. 8, 1966, pp. 205-207.

Sponsored by:

ISBN 978-84-09-43855-6